The Astrophysical Journal, 685:361–375, 2008 September 20

THE RAPIDLY FLARING AFTERGLOW OF THE VERY BRIGHT AND ENERGETIC GRB 070125

Adria C. Updike,[1] Josh B. Haislip,[2] Melissa C. Nysewander,[3] Andrew S. Fruchter,[3] D. Alexander Kann,[4] Sylvio Klose,[4] Peter A. Milne,[5] G. Grant Williams,[6] Weikang Zheng,[7] Carl W. Hergenrother,[8] Jason X. Prochaska,[9] Jules P. Halpern,[10] Nestor Mirabal,[10] John R. Thorstensen,[11] Alexander J. van der Horst,[12] Rhaana L. C. Starling,[13] Judith L. Racusin,[14] David N. Burrows,[14] N. P. M. Kuin,[15] Peter W. A. Roming,[14] Eric Bellm,[16] Kevin Hurley,[16] Weidong Li,[17] Alexei V. Filippenko,[17] Cullen Blake,[18] Dan Starr,[17] Emilio E. Falco,[19] Warren R. Brown,[18] Xinyu Dai,[20] Jinsong Deng,[7] Liping Xin,[7] Yulei Qiu,[7] Jianyan Wei,[7] Yuji Urata,[21,22] Domenico Nanni,[23,24] Elisabetta Maiorano,[25] Eliana Palazzi,[25] Giuseppe Greco,[26] Corrado Bartolini,[26] Adriano Guarnieri,[26] Adalberto Piccioni,[26] Graziella Pizzichini,[25] Federica Terra,[23] Kuntal Misra,[27,28] B. C. Bhatt,[29] G. C. Anupama,[30] X. Fan,[5] L. Jiang,[5] Ralph A. M. J. Wijers,[31] Daniel E. Reichart,[2] Hala A. Eid,[1] Ginger Bryngelson,[1] Jason Puls,[1] R. C. Goldthwaite,[1] and Dieter H. Hartmann[1]

Received 2008 February 4; accepted 2008 May 7

ABSTRACT

We report on multiwavelength observations, ranging from X-ray to radio wave bands, of the IPN-localized gamma-ray burst GRB 070125. Spectroscopic observations reveal the presence of absorption lines due to O I, Si II, and C IV, implying a likely redshift of $z = 1.547$. The well-sampled light curves, in particular from 0.5 to 4 days after the burst, suggest a jet break at 3.7 days, corresponding to a jet opening angle of $\sim 7.0^{\circ}$, and implying an intrinsic GRB energy in the 1–10,000 keV band of around $E_{\gamma} = (6.3-6.9) \times 10^{51}$ ergs (based on the fluences measured by the gamma-ray detectors of the IPN). GRB 070125 is among the brightest afterglows observed to date. The SED implies a host extinction of $A_V < 0.9$ mag. Two rebrightening episodes are observed, one with excellent time coverage, showing an increase in flux of 56% in ~8000 s. The evolution of the afterglow light curve is achromatic at all times. Late-time observations of the afterglow do not show evidence for emission from an underlying host galaxy or supernova. Any host galaxy would be subluminous, consistent with current GRB host galaxy samples. Evidence for strong Mg II absorption features is not found, which is perhaps surprising in view of the relatively high redshift of this burst and the high likelihood for such features along GRB-selected lines of sight.

Subject headings: gamma rays: bursts

Online material: color figures

1. INTRODUCTION

Since the detection of the first gamma-ray burst (GRB) in 1967 with detectors aboard the *Vela* satellites (Klebesadel et al. 1973), our understanding of the nature of this still somewhat mysterious phenomenon went through several major advances. In particular, the establishment of their cosmological distances via ground-based follow-up spectroscopy of their afterglow emission, first accomplished for GRB 970508 (Metzger et al. 1997) at a redshift of $z = 0.835$, led to a spectacular worldwide effort to accumulate prompt and afterglow observations that have yielded

[1] Department of Physics and Astronomy, Clemson University, Clemson, SC 29634.
[2] Department of Physics and Astronomy, University of North Carolina, Chapel Hill, NC 27599.
[3] Space Telescope Science Institute, Baltimore, MD 21218.
[4] Thüringer Landessternwarte Tautenburg, D-07778 Tautenburg, Germany.
[5] Steward Observatory, University of Arizona, Tucson, AZ 85721-0065.
[6] MMT Observatory, University of Arizona, Tucson, AZ 85721-0065.
[7] National Astronomical Observatories, Chaoyang District, Beijing 100012, China.
[8] Lunar and Planetary Laboratory, University of Arizona, Tucson, AZ 85721-0092.
[9] University of California Observatories/Lick Observatory, University of California, Santa Cruz, CA 95064.
[10] Columbia Astrophysics Laboratory, Columbia University, New York, NY 10027.
[11] Department of Physics and Astronomy, Dartmouth College, Hanover, NH 03755-3528.
[12] NASA Postdoctoral Program Fellow, NSSTC, Huntsville, AL 35805.
[13] Department of Physics and Astronomy, University of Leicester, Leicester LE1 7RH, UK.
[14] Department of Astronomy and Astrophysics, Pennsylvania State University, University Park, PA 16802.
[15] Mullard Space Science Laboratory/UCL, Holmbury St. Mary, Dorking, Surrey HR5 6NT, UK.
[16] University of California, Space Sciences Laboratory, Berkeley, CA 94720-7450.
[17] Department of Astronomy, University of California, Berkeley, CA 94720-3411.
[18] Harvard-Smithsonian Center for Astrophysics, Cambridge, MA 02138.
[19] Smithsonian Institution, Whipple Observatory, Amado, AZ 85645.
[20] Department of Physics, Ohio State University, Columbus, OH 43210-1117.
[21] Department of Physics, Saitama University, Shimookubo, Urawa 338-8570, Japan.
[22] Academia Sinica Institute of Astronomy and Astrophysics, Taipei 106, Taiwan.
[23] Second University of Roma "Tor Vergata," Italy.
[24] INAF/OAR.
[25] INAF/IASF Bologna, 40129 Bologna, Italy.
[26] Dipartimento di Astronomia, Universite di Bologna, 40127 Bologna, Italy.
[27] Aryabhatta Research Institute of Observational Sciences (ARIES), Manora Peak, Nainital 263 129, India.
[28] Inter University Center for Astronomy and Astrophysics, Ganeshkhind, Pune 411 007, India.
[29] Center for Research and Education in Science and Technology (CREST), Hosakote, Bangalore 562 114, India.
[30] Indian Institute of Astrophysics, Bangalore 560 034, India.
[31] Astronomical Institute, University of Amsterdam, 1098 SJ Amsterdam, Netherlands.

many surprises and breakthrough discoveries. One decade after the first afterglow was discovered with *BeppoSAX* (Costa et al. 1997; van Paradijs et al. 1997), the accumulated sample of about 500 GRBs[32] exhibits X-ray, optical, and radio afterglows to varying degrees. Their observed redshift distribution (Jakobsson et al. 2006) is very broad, with more than half of the GRBs at distances beyond the peak of the cosmic star formation rate at $z \sim 1$–2, and with GRB 050904 at $z = 6.29$ currently being the most distant burst (Haislip et al. 2006; Kawai et al. 2006). The association of long-duration GRBs with Type Ib/c supernovae (SNe; for a review of SN classification see Filippenko 1997), established in a few cases via direct spectroscopy and in a larger sample via a late extra emission component revealed in broadband photometric observations (e.g., Galama et al. 1998; Hjorth et al. 2003; Stanek et al. 2003; Zeh et al. 2004; Malesani et al. 2004; Pian et al. 2006; Mirabal et al. 2006; Woosley & Bloom 2006), has thus opened promising observational windows into star formation in the universe (e.g., Bromm & Loeb 2006), cosmic chemical evolution via absorption-line spectroscopy of intervening clouds and host galaxies (e.g., Savaglio 2006; Berger et al. 2006), and may eventually provide valuable constraints on the cosmic reionization history in the crucial $z > 6$ epoch (e.g., Fan et al. 2006; Totani et al. 2006; Gallerani et al. 2008; McQuinn et al. 2007). Every new GRB provides yet another opportunity to investigate these topics, or the GRB environment via features in the afterglow power-law decay, or to add key data to enable a better understanding of their statistical properties and morphological classification.

Here we report on follow-up observations of GRB 070125, which was discovered by detectors aboard the IPN members *Mars Odyssey*, *Suzaku*, *INTEGRAL*, Konus-*Wind*, and *RHESSI* at $T_0 =$ 07:20:42 (UT dates and times are used throughout this paper) on 2007 January 25 (Hurley et al. 2007). The Burst Alert Telescope (BAT) detector aboard *Swift* (Gehrels et al. 2004) recorded the burst during a slew and therefore did not trigger. The BAT position is consistent with the IPN localization. The position was monitored with the XRT from 0.54 to 18.5 days after T_0. We report these observations and their implications (see also Racusin et al. 2007b), as well as the results obtained from ground-based follow-up observations with a large group of small-, medium-, and large-aperture telescopes. As observed by *RHESSI*, GRB 070125 had a duration of $T_{90} = 63.0 \pm 1.7$ s (Bellm et al. 2008) and thus clearly belongs in the class of long-soft GRBs (e.g., Kouveliotou et al. 1993). Details of the prompt emission can be found in Bellm et al. (2008). From a joint fit to the *RHESSI* and Konus-*Wind* data, Bellm et al. (2008) derived isotropic energies in the 1 keV–10 MeV band of $(9.44^{+0.40}_{-0.41}) \times 10^{53}$ ergs (Konus-*Wind*) and $(8.27 \pm 0.39) \times 10^{53}$ ergs (*RHESSI*).

Starting with our early response using the 0.9 m SARA telescope and the 2.3 m Bok telescope on Kitt Peak, we compile observations from a large set of follow-up programs to establish the afterglow light-curve properties. We analyze a diverse set of data with a uniform analysis method to reduce any scatter and establish a well-sampled light curve (which is usually not possible with data from a single telescope). We obtained Keck I spectra to establish a burst redshift of $z = 1.547$ (which agrees with the value derived from Gemini-North spectroscopy; Cenko et al. 2008). The afterglow initially appeared to have a jet break around day 1.5, but the analysis presented here shows that at this time multiple rebrightening episodes occur, which are in fact better fitted with abrupt jumps in the flux, and not the usual jet break. However, the available sparse late-time data do indicate that a break in fact does take place, at $\sim$3.7 days after the burst, which agrees with the radio light curve at 4.8 GHz presented here, spanning a time range from 1.5 to 278 days after the burst.

We discuss how these observations place GRB 070125 in the context of other GRBs and how the late-time observations may constrain the properties of the underlying host and a potential SN that is expected to reach its light maximum $\sim 10(1 + z)$ days after gamma-ray emergence. Emission was detected from this source with the Large Binocular Telescope (LBT) at $t = 26.8$ days (Garnavich et al. 2007; Dai et al. 2008), but the flux is too large to be explained with emission from the commonly assumed SN 1998bw–like template at the burst redshift of 1.547, and we instead consider the LBT detection to be the afterglow. This interpretation is supported by a second-epoch LBT observation ($R > 26.1$ mag) that did not result in a detection (Dai et al. 2008).

The paper is organized as follows. In § 2 we describe our set of observations of GRB 070125, from early X-ray and UVOT data from *Swift* to late-time optical observations with the 8.4 m LBT and late-time radio observations with the Westerbork Synthesis Radio Telescope (WSRT). In § 3 we describe the data analysis and results derived from the multiwavelength data, and in § 4 we discuss the implications of this combined data set. In particular, we discuss GRB 070125 in the context of the existing data on afterglow emission properties, and we examine the implied burst energies in light of the standard models for long-soft GRBs and their interactions with the circumburst medium.

2. OBSERVATIONS

GRB 070125 was detected at 07:20:42 on 2007 January 25 by *Mars Odyssey* (HEND and GRS), *Suzaku* (WAM; Yamaoka et al. 2005; K. Yamaoka 2008, in preparation), *INTEGRAL* (SPI-ACS), Konus-*Wind*, and *RHESSI* (Hurley et al. 2007). The *Swift* satellite detected the burst but did not trigger because *Swift* was slewing. The GRB entered the coded field of view of the *Swift* BAT 6 minutes after the trigger time, and ground processing revealed a significant source at the intersection of the IPN annuli, strongly reducing the error box. The BAT (Barthelmy et al. 2005) produced a refined J2000.0 location of $\alpha = 07^{\rm h}51^{\rm m}24^{\rm s}$, $\delta = +31^\circ 08' 24''$ based on data taken about 6 minutes after T_0 (Racusin et al. 2007a). About 13 hr later, *Swift* began observing GRB 070125 as a Target of Opportunity observation. The afterglow was discovered with the Palomar 1.5 m telescope (Cenko & Fox 2007) and produced an accurate afterglow location of $\alpha = 07^{\rm h}51^{\rm m}17^{\rm s}$, $\delta = +31^\circ 09' 04''$ ($\pm 0.5''$ in each coordinate).

Below we describe space-based observations with instruments on the *Swift* satellite, as well as ground-based photometric and spectroscopic observations. Figure 1 shows a false-color image of the field derived from *BVR* observations with the Bok telescope (described in greater detail below). The afterglow shown in the image within the circle has a brightness of $R = 18.7$ mag at 1 day after the burst. The field has a relatively low star density (Galactic coordinates $l = 189.4^\circ$, $b = 25.6^\circ$) and has only a little foreground extinction of $E(B - V) = 0.052$ mag, $A_V = 0.16$ mag (Schlegel et al. 1998).

2.1. *Space-based Observations*

The space-based observations reported in this section consist of ultraviolet, optical, and X-ray data, carried out by the UVOT and XRT instruments on *Swift* beginning 12.97 hr after the burst trigger. The afterglow was detected in the X-ray band and all six UVOT filters, ranging from *V* to UVW2 (central wavelengths of 546 and 193 nm, respectively).

[32] See the compilation in http://www.mpe.mpg.de/~jcg/grbgen.html.

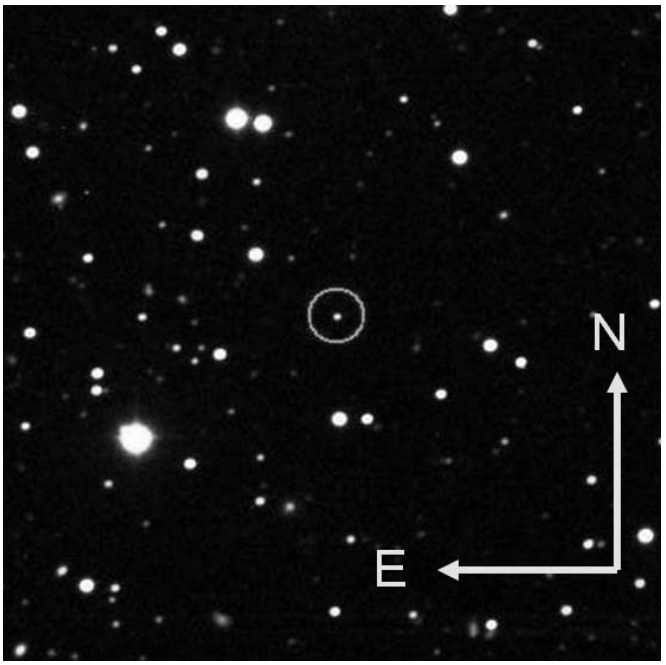

FIG. 1.—Field of GRB 070125 as imaged by the Bok telescope on 2007 January 26 08:11:08 (*BVR*). The field is 6.4′ in diameter. The OT is circled. In this image, north is up and east is to the left. [*See the electronic edition of the Journal for a color version of this figure.*]

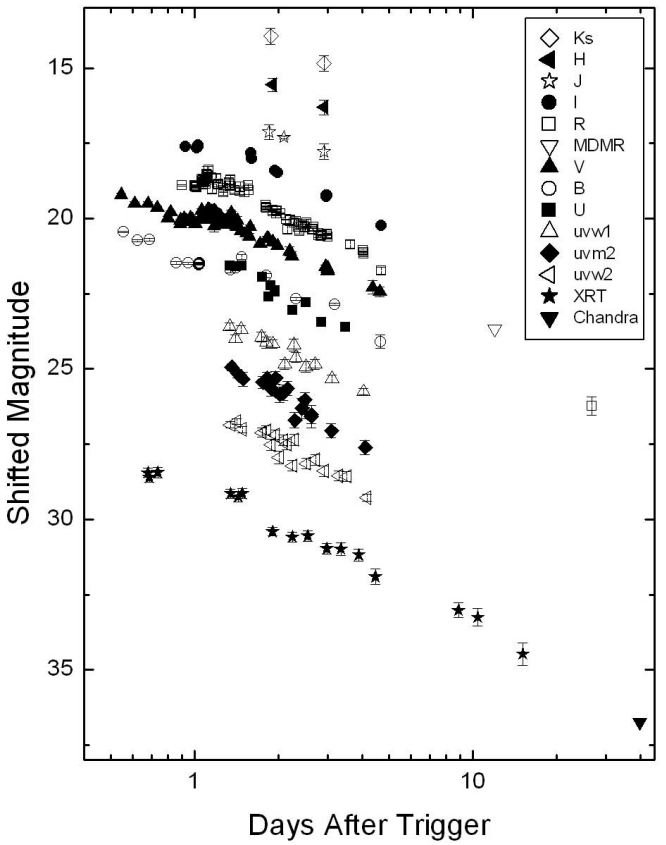

FIG. 2.—Combined data set (Vega magnitude system), corrected for Galactic extinction, arbitrarily scaled with respect to the *R* band for ease in reading. The XRT fluxes have been converted to magnitudes ($m = -2.5 \log F_\nu$). MDM and *Chandra* upper limits are represented by downward-pointing triangles. Band magnitude shifts are $K_s - 3.0$, $H - 2.0$, $J - 1.0$, $I - 0.5$, $V + 1.0$, $B + 2.0$, $U + 3.0$, UVW1 + 5.0, UVM2 + 6.5, and UVW2 + 8.0. All errors (excluding upper limits) are shown.

2.1.1. *XRT Observations*

Although GRB 070125 was detected by the *Swift* BAT in ground analysis, the BAT did not trigger due to the occurrence of the burst during a preplanned slew phase, and consequently the narrow-field instruments did not obtain prompt observations. *Swift* began Target of Opportunity observations of GRB 070125 about 13 hr after the trigger at 20:18:48 2007 January 25.

The X-ray afterglow was initially detected by the XRT (Burrows et al. 2005) in the first few orbits of observation and was followed up for 18.5 days posttrigger until the afterglow was no longer detected by the XRT. The total exposure time of GRB 070125 with the XRT was 170 ks. All observations used the Photon Counting (PC) mode due to the low count rate of the source. Level 1 data products were downloaded from the NASA GSFC *Swift* Data Center (SDC) and processed using XRTDAS software (ver. 2.0.1). The `xrtpipeline` task was used to generate level 2 cleaned event files. Only events with PC grades 0–12 and energies in the range 0.3–10.0 keV were used in subsequent temporal and spectral analysis.

The XRT light curve was created by extracting the counts in a circular region around the afterglow position with a variable radius designed to optimize the signal-to-noise ratio (S/N) depending on the count rate. A region with 40 pixel radius clear of serendipitous background sources was used to estimate the contribution of background counts in the source extraction region. The number of counts per bin was chosen depending on the count rate to show sufficient detail with reasonable error bars. Background-subtracted count rates were also corrected for the portion of the point-spread function (PSF) excluded by the extraction region and any proximity to bad columns and hot pixels in the XRT CCD. Pileup is negligible at these flux levels.

We carried out spectral analysis on this data set to obtain a counts-to-flux conversion for the purpose of creating an XRT light curve in standard units. Spectral analysis was carried out using XSPEC (ver. 12.3.1) and the XRT ancillary response file created with the standard `xrtmkarf` task using the response matrix file swxpc0to12s0_20010101v010.rmf from CALDB (release 2007 December 4). We fitted the spectrum to a simple absorbed power law with an absorption system at $z = 0$ fixed to the Galactic H I column density (4.8×10^{20} cm^{-2}; Dickey & Lockman 1990) and allowed the absorption at the host galaxy redshift ($z = 1.547$) to vary. The resulting fit to the PC spectrum gave an intrinsic effective hydrogen column density of $N_{\rm H} = 0.19^{+0.20}_{-0.18} \times 10^{22}$ cm^{-2} and a photon index of $2.00^{+0.15}_{-0.14}$, with a reduced χ^2 of 0.67 (29 degrees of freedom [dof]). The absorption column is in excess of the Galactic foreground value, suggesting the possibility that the host galaxy or the circumburst medium contributes somewhat to the observed extinction. We address this issue below with the X-ray/optical/near-IR afterglow spectral energy distribution (SED). The mean absorbed (unabsorbed) flux is 3.9×10^{-13} ergs cm^{-2} s^{-1} (4.7×10^{-13} ergs cm^{-2} s^{-1}), with a corresponding mean count rate of 9.0×10^{-3} counts s^{-1}. The resulting light curve is shown (arbitrarily scaled) in Figure 2.

2.1.2. *UVOT Observations*

The UVOT (Roming et al. 2005) began observing 13 hr after the trigger. The data were retrieved from the *Swift* archive at GSFC. Data taken in the UVM2 filter had not all been aspect corrected, but inspection of the individual images showed that the sources fell within their 3″ radius region files. The counts were measured twice, using XIMAGE and UVOTMAGHIST, the latter during testing of the software updates for HEADAS version 6.3.

The measurements were made for 3″ and 5″ radius apertures, both for the transient and for four field stars. Following the recommendations in Poole et al. (2008), an aperture correction was derived based on the observations of field stars having count rates of 1–10 counts s^{-1}, sufficiently low that the PSF is not considered to be affected by the UVOT coincidence loss. The calibration of Poole et al. (2008) was used (CALDB update of 2007 July 11).

Since the UVOT is a photon-counting instrument, subsequent images can be co-added to improve the S/N. This was done by writing software to co-add the counts until a desired value of S/N was found, as well as optimizing the time resolution. We checked that there was no noticeable difference in co-adding counts before or after doing background subtraction or coincidence-loss corrections, as expected for the low count rates of the transient. The measurement error of the UVOT is binomial due to the finite number of frames in an observation, and the errors were calculated accordingly with the formula given by Kuin & Rosen (2008). Magnitudes were derived using the new zero points of Poole et al. (2008).

The UVOT images of GRB 070125 were further reduced following the recipe outlined by Li et al. (2006), which provided an independent photometric calibration to the *U*, *B*, and *V* filters employing a small aperture (radius of 2.5″) for photometry (thus no need to do aperture correction). Comparison between the two reductions indicates that the measurements are consistent with each other within the uncertainties.

2.2. *Ground-based Observations*

2.2.1. *Ground-based Afterglow Photometry*

The GCN burst notice (Hurley et al. 2007) was sent out at 21:46:48 January 25, approximately 13 hr and 26 minutes after the burst had been detected by the IPN. The SARA 0.9 m telescope on Kitt Peak began imaging of the field of GRB 070125 in the *V* band ∼19 hr and 15 minutes after the trigger time and was closely followed by the 0.41 m PROMPT telescope on Cerro Tololo (20 hr and 34 minutes) in *BVRI* and the Bok 2.3 m telescope on Kitt Peak in *V* (24 hr). An afterglow candidate was detected by Cenko & Fox (2007) in the Palomar 1.5 m images. Further observations were obtained with TNT, EST, SOAR, MDM, MMT, Kuiper, Loiano, KAIT, PAIRITEL, TNG, HCT, and the LBT (see Table 1). Observations around 4 days after the trigger were hampered by the full Moon, which may explain why many telescopes stopped observing at that time.

The SARA (Southeastern Association for Research in Astronomy) 0.9 m telescope is located on Kitt Peak. SARA observations were carried out for 3 days following the burst until the afterglow was no longer detectable (Updike et al. 2007). Observations with SARA were limited to the *V* band using the SARA Apogee Alta U47 camera.

The Bok 2.3 m telescope is located at Kitt Peak National Observatory (KPNO) and is operated by the University of Arizona Steward Observatory. Bok observations utilized the 90prime instrument (Williams et al. 2004) and provide *BVRI* data. Supplemental observations were obtained by the Kuiper Mont4k Imager on the Kuiper 1.54 m telescope (located on Mount Bigelow in Arizona) in the *R* band.

PROMPT observations were carried out in *BVRI* by one of the five PROMPT (Panchromatic Optical Monitoring and Polarimetry Telescopes) telescopes located on Cerro Tololo, Chile. PROMPT5 is a 0.41 m Ritchey-Chrétien telescope outfitted with a rapid-readout Apogee Alta U47+ camera (Haislip et al. 2007).

The MDM observations were taken with the 2.4 and 1.3 m Hiltner telescopes on Kitt Peak, a SITe back-side–illuminated CCD, and *VRI* filters.

TABLE 1
OBSERVATIONAL CAMPAIGN

Time	Mag or Flux	Error	Instrument	Band
1.517.....	203	5.5E−5	WSRT	4.8 GHz
5.642.....	102	2.6E−5	WSRT	4.8 GHz
8.634.....	241	2.6E−5	WSRT	4.8 GHz
12.929.....	220	2.6E−5	WSRT	4.8 GHz
13.927.....	−25.0	6.3E−5	WSRT	1.4 GHz
17.916.....	222	2.7E−5	WSRT	4.8 GHz
34.854.....	196	3.0E−5	WSRT	4.8 GHz
50.827.....	240	4.5E−5	WSRT	4.8 GHz
85.730.....	318	4.9E−5	WSRT	4.8 GHz
95.703.....	450	1.0E−4	WSRT	8.4 GHz
170.499.....	157	5.2E−5	WSRT	4.8 GHz
278.204.....	126	7.9E−5	WSRT	4.8 GHz
1.349.....	19.25	0.10	UVOT	UVW2
1.416.....	19.14	0.10	UVOT	UVW2
1.484.....	19.41	0.11	UVOT	UVW2
1.749.....	19.51	0.15	UVOT	UVW2
1.816.....	19.44	0.15	UVOT	UVW2
1.883.....	19.92	0.18	UVOT	UVW2
1.950.....	19.59	0.16	UVOT	UVW2
2.017.....	20.33	0.21	UVOT	UVW2
2.085.....	19.77	0.17	UVOT	UVW2
2.149.....	19.90	0.18	UVOT	UVW2
2.252.....	20.61	0.18	UVOT	UVW2
2.285.....	19.75	0.18	UVOT	UVW2
2.521.....	20.54	0.17	UVOT	UVW2
2.723.....	20.42	0.17	UVOT	UVW2
2.929.....	20.79	0.18	UVOT	UVW2
3.297.....	20.95	0.16	UVOT	UVW2
3.525.....	20.97	0.17	UVOT	UVW2
4.157.....	21.68	0.12	UVOT	UVW2
1.360.....	18.91	0.11	UVOT	UVM2
1.427.....	19.13	0.14	UVOT	UVM2
1.492.....	19.31	0.24	UVOT	UVM2
1.755.....	19.41	0.20	UVOT	UVM2
1.822.....	19.28	0.20	UVOT	UVM2
1.889.....	19.64	0.23	UVOT	UVM2
1.956.....	19.27	0.21	UVOT	UVM2
2.023.....	19.82	0.26	UVOT	UVM2
2.090.....	19.76	0.25	UVOT	UVM2
2.155.....	19.62	0.24	UVOT	UVM2
2.290.....	20.68	0.26	UVOT	UVM2
2.627.....	20.55	0.37	UVOT	UVM2
3.101.....	21.03	0.23	UVOT	UVM2
2.425.....	20.28	0.34	UVOT	UVM2
2.491.....	20.00	0.25	UVOT	UVM2
2.626.....	20.49	0.30	UVOT	UVM2
4.098.....	21.58	0.23	UVOT	UVM2
1.337.....	18.92	0.11	UVOT	UVW1
1.404.....	19.33	0.13	UVOT	UVW1
1.473.....	19.02	0.12	UVOT	UVW1
1.743.....	19.27	0.17	UVOT	UVW1
1.810.....	19.45	0.19	UVOT	UVW1
1.910.....	19.50	0.14	UVOT	UVW1
2.110.....	20.18	0.17	UVOT	UVW1
2.313.....	19.95	0.17	UVOT	UVW1
2.515.....	20.26	0.18	UVOT	UVW1
2.716.....	20.18	0.17	UVOT	UVW1
3.123.....	20.66	0.12	UVOT	UVW1
2.279.....	19.53	0.20	UVOT	UVW1
4.049.....	21.09	0.11	UVOT	UVW1
1.340.....	18.81	0.10	UVOT	*U*
1.408.....	18.83	0.10	UVOT	*U*
1.476.....	18.81	0.10	UVOT	*U*
1.745.....	19.19	0.14	UVOT	*U*
1.845.....	19.85	0.13	UVOT	*U*

TABLE 1—*Continued*

Time	Mag or Flux	Error	Instrument	Band
1.879	19.46	0.16	UVOT	*U*
1.946	19.65	0.17	UVOT	*U*
2.246	20.28	0.10	UVOT	*U*
2.517	20.03	0.13	UVOT	*U*
2.854	20.69	0.09	UVOT	*U*
3.487	20.85	0.08	UVOT	*U*
0.555	18.66	0.03	UVOT	*B*
0.622	18.95	0.04	UVOT	*B*
0.689	18.92	0.04	UVOT	*B*
0.857	19.69	0.05	PROMPT	*B*
0.947	19.70	0.04	PROMPT	*B*
1.034	19.76	0.01	Bok	*B*
1.035	19.72	0.01	Bok	*B*
1.037	19.71	0.01	Bok	*B*
1.038	19.73	0.02	Bok	*B*
1.040	19.71	0.01	Bok	*B*
1.041	19.73	0.01	Bok	*B*
1.042	19.71	0.01	Bok	*B*
1.044	19.69	0.01	Bok	*B*
1.343	19.92	0.09	UVOT	*B*
1.410	19.85	0.09	UVOT	*B*
1.478	19.49	0.08	UVOT	*B*
1.813	20.12	0.07	UVOT	*B*
2.316	20.89	0.05	UVOT	*B*
3.187	21.06	0.04	UVOT	*B*
4.651	22.31	0.22	TNG	*B*
0.545	18.37	0.05	UVOT	*V*
0.611	18.66	0.05	UVOT	*V*
0.679	18.66	0.05	UVOT	*V*
0.736	18.80	0.05	UVOT	*V*
0.802	19.15	0.07	SARA	*V*
0.821	18.95	0.04	SARA	*V*
0.889	19.33	0.05	SARA	*V*
0.891	19.21	0.02	PROMPT	*V*
0.914	19.15	0.05	SARA	*V*
0.935	19.23	0.04	SARA	*V*
0.957	19.28	0.04	SARA	*V*
0.967	19.14	0.04	PROMPT	*V*
0.981	19.21	0.04	SARA	*V*
1.007	19.33	0.03	SARA	*V*
1.046	19.20	0.01	Bok	*V*
1.049	19.15	0.01	Bok	*V*
1.051	19.15	0.01	Bok	*V*
1.052	19.15	0.01	Bok	*V*
1.054	19.15	0.02	Bok	*V*
1.055	19.16	0.01	Bok	*V*
1.056	19.17	0.01	Bok	*V*
1.058	19.15	0.02	Bok	*V*
1.059	19.14	0.02	Bok	*V*
1.063	18.88	0.05	SARA	*V*
1.063	19.13	0.01	Bok	*V*
1.066	19.12	0.01	Bok	*V*
1.071	19.06	0.04	SARA	*V*
1.078	19.05	0.04	SARA	*V*
1.083	19.07	0.01	Bok	*V*
1.084	19.08	0.01	Bok	*V*
1.087	19.06	0.01	Bok	*V*
1.088	19.20	0.05	SARA	*V*
1.088	19.04	0.01	Bok	*V*
1.090	19.05	0.01	Bok	*V*
1.091	19.04	0.01	Bok	*V*
1.094	19.02	0.01	Bok	*V*
1.095	19.03	0.01	Bok	*V*
1.097	19.04	0.01	Bok	*V*
1.098	19.04	0.01	Bok	*V*
1.099	18.98	0.06	SARA	*V*

TABLE 1—*Continued*

Time	Mag or Flux	Error	Instrument	Band
1.099	19.03	0.01	Bok	*V*
1.102	18.99	0.02	Bok	*V*
1.103	19.00	0.01	Bok	*V*
1.105	19.00	0.01	Bok	*V*
1.106	18.98	0.01	Bok	*V*
1.108	19.04	0.05	SARA	*V*
1.108	18.98	0.01	Bok	*V*
1.109	18.98	0.02	Bok	*V*
1.110	18.97	0.01	Bok	*V*
1.113	18.90	0.03	Bok	*V*
1.115	18.90	0.03	Bok	*V*
1.117	19.05	0.06	SARA	*V*
1.118	18.85	0.04	Bok	*V*
1.120	18.90	0.03	Bok	*V*
1.123	18.92	0.03	Bok	*V*
1.125	18.88	0.03	Bok	*V*
1.128	18.87	0.03	Bok	*V*
1.130	18.91	0.03	Bok	*V*
1.132	18.92	0.03	Bok	*V*
1.135	18.96	0.02	Bok	*V*
1.137	19.19	0.05	SARA	*V*
1.137	18.97	0.03	Bok	*V*
1.140	18.98	0.01	Bok	*V*
1.143	18.95	0.02	Bok	*V*
1.145	18.96	0.03	Bok	*V*
1.148	18.95	0.04	Bok	*V*
1.150	18.92	0.03	Bok	*V*
1.164	19.08	0.02	SARA	*V*
1.164	18.96	0.04	Bok	*V*
1.166	19.13	0.20	TNT 0.8 m	*V*
1.166	18.92	0.02	Bok	*V*
1.169	18.97	0.04	Bok	*V*
1.172	18.98	0.02	Bok	*V*
1.175	19.01	0.02	Bok	*V*
1.175	19.40	0.20	TNT 0.8 m	*V*
1.178	19.03	0.02	Bok	*V*
1.180	18.91	0.03	SARA	*V*
1.180	18.98	0.02	Bok	*V*
1.183	18.97	0.02	Bok	*V*
1.186	18.98	0.15	TNT 0.8 m	*V*
1.186	19.01	0.03	Bok	*V*
1.193	18.94	0.04	SARA	*V*
1.194	19.07	0.15	TNT 0.8 m	*V*
1.209	19.16	0.05	SARA	*V*
1.210	19.03	0.02	Bok	*V*
1.213	19.08	0.01	Bok	*V*
1.215	19.06	0.01	Bok	*V*
1.219	19.07	0.01	Bok	*V*
1.221	19.07	0.02	Bok	*V*
1.224	19.11	0.02	Bok	*V*
1.224	19.06	0.04	SARA	*V*
1.226	19.07	0.02	Bok	*V*
1.227	19.14	0.10	TNT 0.8 m	*V*
1.229	19.09	0.02	Bok	*V*
1.231	19.06	0.01	Bok	*V*
1.234	19.14	0.02	Bok	*V*
1.236	19.14	0.02	Bok	*V*
1.241	19.10	0.10	TNT 0.8 m	*V*
1.241	19.10	0.07	EST 1 m	*V*
1.258	19.35	0.12	TNT 0.8 m	*V*
1.287	19.28	0.12	TNT 0.8 m	*V*
1.288	19.37	0.10	EST 1 m	*V*
1.299	19.23	0.12	TNT 0.8 m	*V*
1.312	19.24	0.12	TNT 0.8 m	*V*
1.355	18.98	0.11	UVOT	*V*
1.360	19.07	0.14	TNT 0.8 m	*V*

TABLE 1—*Continued*

Time	Mag or Flux	Error	Instrument	Band
1.376.....	19.12	0.12	TNT 0.8 m	*V*
1.411.....	19.38	0.12	TNT 0.8 m	*V*
1.422.....	19.44	0.12	UVOT	*V*
1.423.....	19.22	0.13	TNT 0.8 m	*V*
1.472.....	19.57	0.13	TNT 0.8 m	*V*
1.536.....	19.64	0.20	TNT 0.8 m	*V*
1.572.....	19.76	0.10	HCT	*V*
1.582.....	19.44	0.06	HCT	*V*
1.721.....	20.00	0.07	UVOT	*V*
1.822.....	19.81	0.06	SARA	*V*
1.848.....	19.83	0.05	PROMPT	*V*
1.914.....	19.93	0.05	SARA	*V*
1.987.....	20.07	0.01	MDM	*V*
2.199.....	20.24	0.15	TNT 0.8 m	*V*
2.237.....	20.40	0.14	TNT 0.8 m	*V*
2.964.....	20.76	0.05	SARA	*V*
3.000.....	20.88	0.02	MDM	*V*
3.003.....	20.81	0.02	MDM	*V*
3.006.....	20.91	0.03	MDM	*V*
3.008.....	20.89	0.02	MDM	*V*
4.356.....	21.45	0.22	HCT	*V*
4.642.....	21.60	0.16	TNT 0.8 m	*V*
0.900.....	18.76	0.02	PROMPT	*R*
0.998.....	18.78	0.02	Bok	*R*
0.999.....	18.80	0.02	Bok	*R*
1.001.....	18.77	0.02	Bok	*R*
1.002.....	18.80	0.01	Bok	*R*
1.003.....	18.80	0.01	Bok	*R*
1.005.....	18.79	0.02	Bok	*R*
1.006.....	18.81	0.02	Bok	*R*
1.008.....	18.80	0.01	Bok	*R*
1.009.....	18.78	0.01	Bok	*R*
1.010.....	18.78	0.02	Bok	*R*
1.019.....	18.81	0.02	Bok	*R*
1.013.....	18.79	0.01	Bok	*R*
1.015.....	18.80	0.02	Bok	*R*
1.016.....	18.84	0.01	Bok	*R*
1.017.....	18.84	0.02	Bok	*R*
1.019.....	18.83	0.02	Bok	*R*
1.063.....	18.61	0.21	KAIT	*R*
1.065.....	18.60	0.16	KAIT	*R*
1.070.....	18.75	0.11	KAIT	*R*
1.070.....	18.59	0.11	KAIT	*R*
1.075.....	18.67	0.09	KAIT	*R*
1.078.....	18.66	0.07	KAIT	*R*
1.081.....	18.68	0.07	KAIT	*R*
1.084.....	18.63	0.07	KAIT	*R*
1.087.....	18.60	0.08	KAIT	*R*
1.087.....	18.66	0.08	KAIT	*R*
1.093.....	18.59	0.08	KAIT	*R*
1.095.....	18.63	0.08	KAIT	*R*
1.095.....	18.71	0.08	KAIT	*R*
1.102.....	18.40	0.13	KAIT	*R*
1.104.....	18.42	0.10	KAIT	*R*
1.104.....	18.51	0.14	KAIT	*R*
1.110.....	18.41	0.27	KAIT	*R*
1.120.....	18.44	0.11	KAIT	*R*
1.120.....	18.58	0.15	KAIT	*R*
1.125.....	18.26	0.12	KAIT	*R*
1.151.....	18.52	0.14	TNT 0.8 m	*R*
1.159.....	18.88	0.17	TNT 0.8 m	*R*
1.201.....	18.53	0.13	TNT 0.8 m	*R*
1.209.....	18.76	0.10	TNT 0.8 m	*R*
1.222.....	18.71	0.10	EST 1 m	*R*
1.266.....	19.00	0.10	EST 1 m	*R*
1.273.....	18.85	0.09	TNT 0.8 m	*R*

TABLE 1—*Continued*

Time	Mag or Flux	Error	Instrument	Band
1.331.....	18.68	0.15	TNT 0.8 m	*R*
1.339.....	18.79	0.15	TNT 0.8 m	*R*
1.343.....	18.58	0.15	TNT 0.8 m	*R*
1.346.....	18.74	0.16	TNT 0.8 m	*R*
1.394.....	18.93	0.10	TNT 0.8 m	*R*
1.450.....	18.96	0.10	TNT 0.8 m	*R*
1.462.....	18.82	0.17	TNT 0.8 m	*R*
1.513.....	19.00	0.14	TNT 0.8 m	*R*
1.555.....	18.77	0.06	HCT	*R*
1.563.....	18.92	0.02	HCT	*R*
1.796.....	19.43	0.05	Kuiper	*R*
1.802.....	19.49	0.04	Kuiper	*R*
1.807.....	19.53	0.05	Kuiper	*R*
1.813.....	19.52	0.04	Kuiper	*R*
1.905.....	19.58	0.03	PROMPT	*R*
1.912.....	19.63	0.02	Kuiper	*R*
1.964.....	19.60	0.04	MDM	*R*
1.968.....	19.70	0.02	MDM	*R*
1.971.....	19.64	0.02	MDM	*R*
1.975.....	19.64	0.01	MDM	*R*
1.979.....	19.64	0.01	MDM	*R*
1.983.....	19.61	0.02	MDM	*R*
2.036.....	19.70	0.01	Kuiper	*R*
2.130.....	19.90	0.01	Kuiper	*R*
2.160.....	20.23	0.15	TNT 0.8 m	*R*
2.213.....	19.93	0.18	EST 1 m	*R*
2.275.....	20.00	0.11	TNT 0.8 m	*R*
2.312.....	19.97	0.10	TNT 0.8 m	*R*
2.350.....	20.15	0.10	TNT 0.8 m	*R*
2.387.....	20.29	0.10	TNT 0.8 m	*R*
2.427.....	20.10	0.10	TNT 0.8 m	*R*
2.464.....	20.07	0.10	TNT 0.8 m	*R*
2.500.....	20.17	0.12	TNT 0.8 m	*R*
2.533.....	20.01	0.12	TNT 0.8 m	*R*
2.644.....	20.25	0.04	Loiano	*R*
2.659.....	20.23	0.05	Loiano	*R*
2.677.....	20.16	0.04	Loiano	*R*
2.781.....	20.44	0.06	Loiano	*R*
2.795.....	20.36	0.04	Loiano	*R*
2.843.....	20.46	0.04	Kuiper	*R*
2.854.....	20.42	0.03	Kuiper	*R*
2.865.....	20.40	0.02	Kuiper	*R*
2.989.....	20.40	0.02	MDM	*R*
2.992.....	20.38	0.02	MDM	*R*
2.995.....	20.40	0.02	MDM	*R*
2.997.....	20.41	0.02	MDM	*R*
3.006.....	20.47	0.03	Kuiper	*R*
3.631.....	20.73	0.14	Loiano	*R*
4.034.....	20.92	0.04	MDM	*R*
4.038.....	21.00	0.03	MDM	*R*
4.042.....	20.99	0.05	MDM	*R*
4.046.....	21.03	0.05	MDM	*R*
4.678.....	20.97	0.12	TNG	*R*
4.866.....	22.23	0.08	Kuiper	*R*
12.001.....	23.80	Upper limit	MDM	*R*
26.800.....	26.10	0.30	LBT	*R*
0.929.....	18.21	0.02	PROMPT	*I*
1.020.....	18.25	0.02	Bok	*I*
1.022.....	18.22	0.02	Bok	*I*
1.023.....	18.23	0.03	Bok	*I*
1.025.....	18.21	0.03	Bok	*I*
1.026.....	18.21	0.02	Bok	*I*
1.028.....	18.19	0.03	Bok	*I*
1.029.....	18.19	0.03	Bok	*I*
1.030.....	18.17	0.03	Bok	*I*
1.039.....	18.15	0.03	Bok	*I*

TABLE 1—*Continued*

Time	Mag or Flux	Error	Instrument	Band
1.591	18.41	0.09	HCT	*I*
1.599	18.61	0.09	HCT	*I*
1.947	19.01	0.05	PROMPT	*I*
1.992	19.08	0.02	MDM	*I*
2.977	19.88	0.02	MDM	*I*
2.980	19.82	0.02	MDM	*I*
2.982	19.82	0.03	MDM	*I*
4.693	20.84	0.06	TNG	*I*
1.854	18.17	0.24	SOAR	*J*
2.090	18.35	0.04	MMT	*J*
2.916	18.82	0.26	PAIRITEL	*J*
1.907	17.58	0.22	SOAR	*H*
2.916	18.33	0.25	PAIRITEL	*H*
1.877	16.96	0.28	SOAR	K_s
2.916	17.86	0.25	PAIRITEL	K_s
0.550	5.44E−12	4.95E−13	XRT	X
0.610	4.23E−12	6.47E−13	XRT	X
0.621	3.51E−12	5.30E−13	XRT	X
0.679	4.16E−12	6.36E−13	XRT	X
0.688	3.62E−12	5.70E−13	XRT	X
0.737	4.19E−12	7.12E−13	XRT	X
1.349	2.19E−12	3.41E−13	XRT	X
1.437	2.00E−12	3.23E−13	XRT	X
1.483	2.19E−12	3.61E−13	XRT	X
1.909	6.85E−13	9.24E−14	XRT	X
2.248	5.83E−13	9.04E−14	XRT	X
2.552	6.01E−13	1.09E−13	XRT	X
2.988	4.08E−13	7.35E−14	XRT	X
3.359	4.05E−13	8.70E−14	XRT	X
3.896	3.37E−13	6.75E−14	XRT	X
4.470	1.73E−13	4.86E−14	XRT	X
8.884	6.21E−14	1.55E−14	XRT	X
10.423	4.99E−14	1.55E−14	XRT	X
15.139	1.62E−14	6.75E−15	XRT	X
39.760	2E−15	Upper limit	*Chandra*	X

NOTES.—Observations carried out by this collaboration, late-time LBT detection (Dai et al. 2008), and late-time *Chandra* observation (Cenko et al. 2007). X-ray fluxes have units of ergs cm^{-2} s^{-1}. Radio fluxes are given in μJy.

Observations from the Loiano 1.52 m telescope of the Bologna Astronomical Observatory, located at Loiano (Italy), were taken in the Cousins *R* band equipped with BFOSC, a multipurpose instrument for imaging and spectroscopy (Greco et al. 2007).

The 0.8 m TNT telescope and 1 m EST telescope are located at Xinglong Observatory of the National Astronomical Observatories of China. Each telescope is equipped with a Princeton Instruments 1340×1300 pixel CCD. Observations were carried out in the *R* and *V* bands. Observational details can be found in Deng & Zheng (2006).

The 3.58 m Telescopio Nazionale Galileo (TNG) is located at La Palma in the Canary Islands (Spain). TNG was equipped with the spectrophotometer DOLoRES (Device Optimized for the Low Resolution) operating in imaging mode with a scale of $0.275''$ $pixel^{-1}$.

The KAIT (Katzman Automatic Imaging Telescope; Filippenko et al. 2001) 0.76 m data are unfiltered and were obtained with an Apogee AP7 camera. Li et al. (2003) demonstrated that the KAIT unfiltered magnitudes can be reliably transformed to the standard Cousins *R* band with a precision of ~5%, if the color of the object is known. Since we have reliable color information for GRB 070125 during the time of the KAIT observations, we calibrated the KAIT data to the *R* band following the procedure in Li et al. (2003).

The SOAR (Southern Observatory for Astrophysical Research) 4.1 m telescope is located on Cerro Pachon, Chile. SOAR observations were taken in the near-IR using OSIRIS (Ohio State Infrared Imager/Spectrometer).

PAIRITEL (Peters Automated Infrared Imaging Telescope) is a 1.3 m telescope located on Mount Hopkins in Arizona. It is a robotic telescope that allows for rapid follow-up IR imaging of GRB targets. The PAIRITEL observations were taken in the near-IR using a Two Micron All Sky Survey instrument.

The MMT is located at the Whipple Observatory on Mount Hopkins in Arizona. It is a 6.5 m telescope that contributed near-IR observations, obtained with SWIRC, the SAO Widefield Infrared Camera.

Optical observations of the afterglow were carried out by the 2.01 m Himalayan Chandra Telescope (HCT) at the Indian Astronomical Observatory (IAO), Hanle (India). The CCD used at HCT was a 2048×4096 pixel SITe chip mounted on the Himalayan Faint Object Spectrograph Camera (HFOSC). Filters used are Bessell *V*, *R*, and *I*.

The images were reduced and stacked where appropriate. Optical calibration was performed using IRAF PSF photometry and comparison to 15 standard stars, whose magnitudes were obtained through a field calibration using Graham standard stars (Graham 1982) and the Hardie method (Hiltner 1964). Near-IR images were reduced in IRAF using standard reduction pipelines. The MMT images were calibrated relative to standards observed during the same night, and the SOAR images were calibrated relative to the Graham standard stars. LBT data cited are derived from Garnavich et al. (2007) and Dai et al. (2008). Note that the Sloan r' observation has been converted to the *R* band. All observations carried out by this collaboration can be found in Table 1.

2.2.2. *Ground-based Afterglow Spectroscopy*

We observed the afterglow of GRB 070125 with the Keck I LRIS double spectrograph (Oke et al. 1995) through a long slit $1.0''$ wide starting at 05:44:05 on January 26. Two 600 s exposures were acquired using the D560 dichroic, the 400/3400 grism, and the 600/5000 grating. This instrumental configuration yields nearly continuous spectra over the range 3000–8000 Å at a spectral resolution (full width at half-maximum intensity; FWHM) of ~8 Å on the blue side and ~6 Å on the red side. The data were reduced using standard procedures (bias subtracted, flat-fielded) and extracted with a boxcar encompassing ~90% of the flux.

2.2.3. *Ground-based Radio Observations*

Radio observations were performed with the WSRT at 1.4, 4.8, and 8.4 GHz. We used the Multi Frequency Front Ends (Tan 1991) in combination with the IVC+DZB back end[33] in continuum mode, with a bandwidth of 8×20 MHz. Gain and phase calibrations were performed with the calibrator 3C 286. The first observation at 4.8 GHz, 1.5 days after the burst, was reported as a nondetection with a 3 σ upper limit of 261 μJy (van der Horst 2007a), but a careful reanalysis of the data resulted in a 3.7σ detection. The radio afterglow detection at ~5 days was reported by Chandra & Frail (2007) and van der Horst (2007b) using the Very Large Array at 8.64 GHz and the WSRT at 4.8 GHz, respectively. The afterglow was bright enough to be detected up to 170 days after the burst at 4.8 GHz; after that, the flux dropped below the sensitivity limit. The measurement at 1.4 GHz resulted in a nondetection, while at 8.4 GHz we had a clear detection at 95 days

[33] See § 5.2 at http://www.astron.nl/wsrt/wsrtGuide/node6.html.

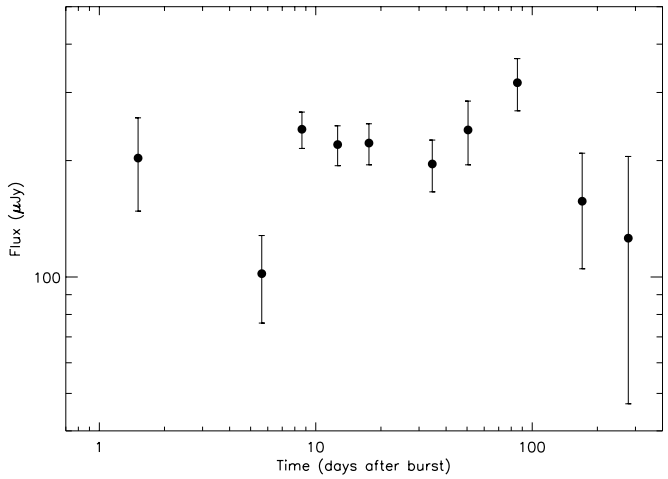

FIG. 3.—WSRT observations of GRB 070125 at 4.8 GHz.

after the burst. The details of our observations are shown in Table 1; the 4.8 GHz light curve is shown in Figure 3.

3. DATA ANALYSIS AND RESULTS

3.1. *The Light Curve*

The light curve (Fig. 2) combines our optical, near-IR, and *Swift* data. The bands have been offset from their actual magnitudes for ease in reading. The original unextinguished magnitudes are listed in Table 1. Throughout this paper we assume a standard flat cold dark matter cosmology (ΛCDM), with parameters $(\Omega_\Lambda, \Omega_M, H_0) = (0.761, 0.239, 73\ \mathrm{km\ s^{-1}\ Mpc^{-1}})$, as found in the third-year *WMAP* data release (Spergel et al. 2007) assuming large-scale structure traced by luminous red galaxies (Tegmark et al. 2006). The particular set of values corresponds to the "Vanilla model" of Tegmark et al. (2006).

3.2. *Fitting the Light Curve*

Swift observations began 0.54 days after the burst, followed by ground-based observations beginning 0.8 days later by the SARA telescope, closely followed by the rest of the various telescopes collected in this collaborative effort. Due to a lack of early coverage, it is not immediately clear whether or not there is a jet break. We fit a broken power-law decay to each band separately using the Beuermann function (Beuermann et al. 1999) as revised by Rhoads & Fruchter (2001):

$$F_\nu(t) = 2^{1/n} F_\nu(t_b) \left[\left(\frac{t}{t_b} \right)^{\alpha_1 n} + \left(\frac{t}{t_b} \right)^{\alpha_2 n} \right]^{-1/n}, \qquad (1)$$

where F is the flux density in band ν, $F_\nu(t_b)$ is the flux density in band ν at the break time, α_1 and α_2 are the slopes of the power-law decay (before and after the jet break, respectively), and n is the smoothness of the curve at the break.

The complicated shape of our light curve (see Fig. 4) makes fitting the overall structure difficult. By using the flux at 2 days, we shifted all bands to the extinction-corrected R band for comparison and fitting. The entire data set is obviously not well fitted by a broken power-law function. Rapid flaring observed between 1 and 2 days posttrigger (§ 3.5) influences the fit. Broken power-law fits to the optical/UV/near-IR data set and the X-ray data set showed that this was indeed a poor model to the data set. In addition, this fit predicted that the afterglow would have been nearly

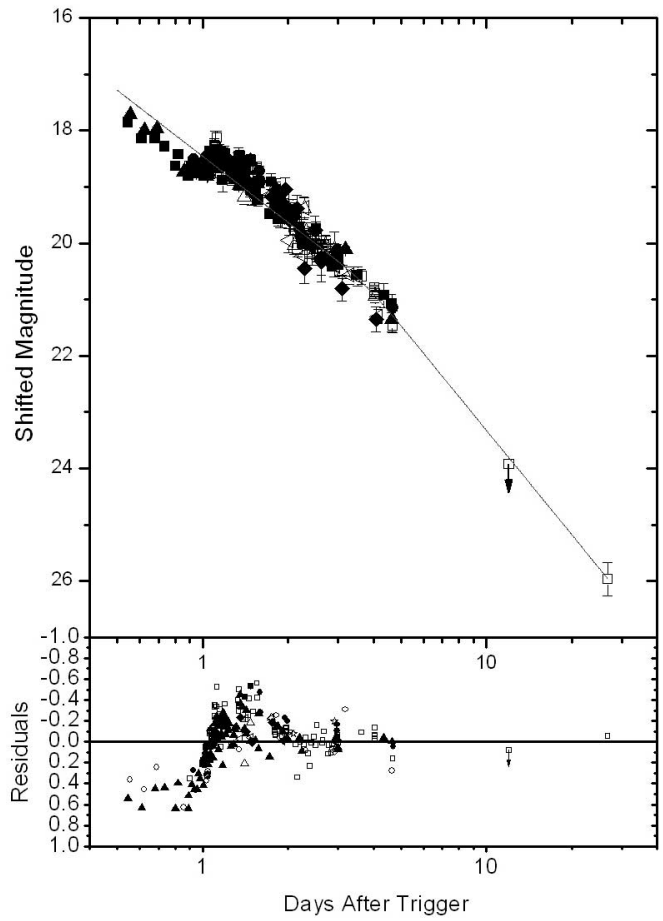

FIG. 4.—All UV, optical, and near-IR data contained in Fig. 2 have been shifted to the R band based on the flux at 2 days posttrigger. Data before 2 days have been removed from this fit due to rapid flaring. The residuals to the fit are shown. We derive a jet break time of 3.73 ± 0.52 days. [*See the electronic edition of the Journal for a color version of this figure.*]

a magnitude brighter than it was observed to be at 26.8 days. This would suggest the need for a second, nonstandard jet break after 4 days.

By eliminating the flaring region between 1 and 2 days after the trigger, we can better constrain our fit. However, the best fit was determined by only considering the data taken after 2 days. At this point, it appears as if the flaring has settled to the point where the best estimate for the break time can be made. From the optical/UV/near-IR data set after 2 days, we determine an $\alpha_1 = 1.56 \pm 0.27$, $\alpha_2 = 2.47 \pm 0.13$, and a jet break time of $t = 3.73 \pm 0.52$ days. While the X-ray data do not require a break before 9 days, they are also not inconsistent with a break (see Table 2). Lack of an achromatic break is not an uncommon feature in *Swift*-era bursts (e.g., Curran et al. 2007). The results of all of the fits to the optical/UV/near-IR and X-ray data can be found in Table 2.

Late-time MDM, LBT, and *Chandra* observations (Cenko et al. 2007) were invaluable in the determination of a late jet break time, as were the numerous early observations that allowed us to resolve the early flaring activity so as not to be confused with a jet break. While the late MDM upper limit implied an optical jet break, the LBT detection at 26.8 days posttrigger confirmed the existence of a jet break. Second-epoch deep imaging of the field of GRB 070125 by the LBT did not result in the further detection of the source, thus allowing us to interpret the first detection as the afterglow (Dai et al. 2008). Late-time *Chandra* X-Ray Telescope

TABLE 2
Light-Curve Fitting

Band	Model	α_1	α_2	Break Time	χ^2/dof
Opt/UV/NIR.....	All data	0.47 ± 0.10	2.05 ± 0.04	1.39 ± 0.04	10.25
	No flaring	1.24 ± 0.09	2.49 ± 0.13	3.37 ± 0.36	3.35
	After 2 days	1.56 ± 0.27	2.47 ± 0.13	3.73 ± 0.52	2.98
X-ray	All data	$1.16^{+0.23}_{-0.87}$	$1.85^{+0.19}_{-0.15}$	$1.34^{+0.24}_{-0.51}$	1.6
	No flaring	$1.49^{+0.14}_{-0.09}$	$1.94^{+0.39}_{-0.30}$	$3.93^{+9.72}_{-1.85}$	0.80
	After 2 days	$1.0^{+0.62}_{-1.81}$	$1.99^{+0.46}_{-0.32}$	$3.34^{+9.03}_{-1.27}$	0.50

Notes.—Results of fitting a Beuermann function (Beuermann et al. 1999; as revised by Rhoads & Fruchter 2001) broken power-law function to the data set; Opt/UV/NIR refers to the combined data set of optical, UV, and near-IR data. The columns labeled "No flaring" have removed the data between 1 and 2 days from the fit.

observations also imply a late jet break in the X-ray light curve. The *Chandra* upper limit of 2×10^{-15} ergs cm^{-2} s^{-1} (Cenko et al. 2007) at 39.76 days after the burst was obtained in the 0.3–10 keV energy range and is thus directly comparable to the XRT observations. Fits to the XRT data (Table 2) do not include this upper limit.

The fluence of the burst was measured independently by the Konus-*Wind* and *RHESSI* instruments. By extrapolating to the GRB rest-frame energy band of 1 keV–10 MeV, we infer an isotropic energy of $E_{\rm iso,\,Konus} = (9.44^{+0.40}_{-0.41}) \times 10^{53}$ ergs and $E_{\rm iso,\,RHESSI} = (8.27 \pm 0.39) \times 10^{53}$ ergs (Bellm et al. 2008). Assuming a jet break at $t = 3.73$ days and using the equations described in Sari et al. (1999), including a circumburst density of $n = 3$ cm^{-3} and a gamma-ray efficiency of $\eta_\gamma = 0.2$ (Bellm et al. 2008), we find a jet half-opening angle of $\theta_{j,\,\rm Konus} = 5.65^\circ \pm 0.03^\circ$ or $\theta_{j,\,RHESSI} = 5.74^\circ \pm 0.04^\circ$. For a jet break time of 3.73 days, the corresponding collimated energy emission is $E_{\gamma,\,\rm Konus} = 4.58^{+0.24}_{-0.25} \times 10^{51}$ ergs or $E_{\gamma,\,RHESSI} = (4.15 \pm 0.25) \times 10^{51}$ ergs following Bloom et al. (2003).

Comprehensive broadband and energetics modeling of GRB 070125 was presented by Chandra et al. (2008). They derived a circumburst density of $n \sim 50$ cm^{-3} from the kinetic energy and $n = 15.7$ cm^{-3} from a broadband fit using the synchrotron model. If we use $n = 50$ cm^{-3} to calculate E_γ, we find $E_{\gamma,\,\rm Konus} = 9.26^{+0.49}_{-0.50} \times 10^{51}$ ergs ($\theta_{j,\,\rm Konus} = 8.03^\circ \pm 0.04^\circ$) and $E_{\gamma,\,RHESSI} = (8.39 \pm 0.50) \times 10^{51}$ ergs ($\theta_{j,\,RHESSI} = 8.16^\circ \pm 0.05^\circ$). Using the broadband fit $n = 15.7$ cm^{-3}, we derive $E_{\gamma,\,\rm Konus} = 6.93^{0.37}_{0.38} \times 10^{51}$ ergs ($\theta_{j,\,\rm Konus} = 6.94^\circ \pm 0.03^\circ$) and $E_{\gamma,\,RHESSI} = (6.28 \pm 0.37) \times 10^{51}$ ergs ($\theta_{j,\,RHESSI} = 7.07^\circ \pm 0.04^\circ$). The most plausible value for the circumburst density comes from the broadband fit, so the energies derived from $n = 15.7$ will be quoted as the energy of the burst in this paper.

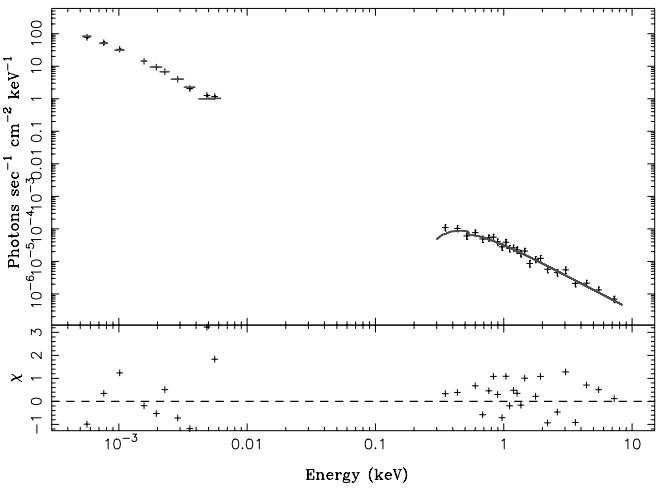

Fig. 5.—Unfolded SED at 4.26 days since trigger, including a *Swift* XRT spectrum and near-IR/optical/UV photometry (*black plus signs, top panel*). The line indicates the best-fitting model of an absorbed, broken power law plus LMC-like extinction. The bottom panel shows the residuals of the fit. [*See the electronic edition of the Journal for a color version of this figure*.]

At $z = 1.547$, a jet break at 3.73 days (Fig. 4) implies a rather large energy release (when placed in the context of the sample studied by Bloom et al. 2003). Both the observations of Konus-*Wind* and *RHESSI* imply that GRB 070125 is one of the most energetic bursts discovered to date (Bloom et al. 2003).

3.3. *Spectral Energy Distribution*

Due to the variable nature of the early-time light curve, special care was used in determining the SED. We used the method employed by Kann et al. (2006) for deriving the SED of GRB 030329. Using the *R*-band light curve as a reference, the other optical, UV, and near-IR bands were shifted until they matched the *R*-band light curve, which assumes the achromaticity already demonstrated above. Since we find no evidence for color evolution, use of the method is reasonable. The SED is then determined from the different colors, such as $U - R$. The *R*-band value is arbitrary, and thus also the absolute flux density scale of the SED. Also, due to achromaticity, no specific time should be associated with the SED shown in Figure 5. To model the intrinsic optical extinction, we use the three best-modeled extinction curves: those of the Milky Way (MW), Large Magellanic Cloud (LMC), and Small Magellanic Cloud (SMC) as parameterized by Pei (1992). We fit the SED with the method described by Kann et al. (2006). The results are given in Table 3. We find a clear preference for the SMC dust model ($A_V = 0.11 \pm 0.04$ mag). This preference, as well as the intrinsic spectral slope β and the small host galaxy extinction A_V, are all typical for the afterglows of (long) GRBs (e.g., Kann et al. 2006, 2007; Starling et al. 2007; Schady et al. 2007).

We combined the optical, UV, and near-IR photometry at, or extrapolated to, 4.26 days posttrigger with an X-ray spectrum

TABLE 3
UV/Optical/NIR Spectral Energy Distribution

Dust	χ^2/dof	β	A_V (mag)
None.....	2.615	0.854 ± 0.036	None
MW	3.137	0.855 ± 0.058	0.00 ± 0.032
LMC.....	2.643	0.736 ± 0.129	0.067 ± 0.070
SMC	0.896	0.519 ± 0.104	0.139 ± 0.041

Notes.—SED for UV, optical, and near-IR data only. We see that the SMC dust is strongly preferred.

TABLE 4
X-Ray/UV/Optical/NIR Spectral Energy Distribution

Model	Γ_1	E_{bk} (keV)	Γ_2	$E(B-V)$ (mag)	N_H (10^{21} cm^{-2})	χ^2/dof
PL+MW	1.99 ± 0.01	...	...	$0^{+8\times10^{-4}}_{-0}$	$2.5^{+1.6}_{-1.3}$	3.74
PL+LMC	1.99 ± 0.01	...	...	$0^{+8\times10^{-4}}_{-0}$	$2.5^{+1.6}_{-1.3}$	3.74
PL+SMC	1.99 ± 0.01	...	...	$0^{+9\times10^{-4}}_{-0}$	$2.5^{+1.6}_{-1.3}$	3.74
BKNPL+MW	1.6 ± 0.1	0.0019 ± 0.0002	2.03 ± 0.03	<0.02	$1.4^{+1.6}_{-1.3}$	1.72
BKNPL+LMC	1.5 ± 0.1	0.0023 ± 0.0001	$2.06^{+0.03}_{-0.02}$	0.03 ± 0.01	1.8 ± 1.3	1.17
BKNPL+SMC	1.6 ± 0.1	$0.0024^{+0.0002}_{-0.0004}$	$2.06^{+0.02}_{-0.03}$	$0.02^{+0.04}_{-0.01}$	$1.8^{+1.7}_{-1.3}$	1.31
BKNPL+MW	$\Gamma_2 - 0.5$	0.0019 ± 0.0002	$2.04^{+0.03}_{-0.02}$	0.02 ± 0.01	$1.3^{+1.6}_{-1.2}$	1.73
BKNPL+LMC	$\Gamma_2 - 0.5$	$0.0023^{+0.0001}_{-0.0002}$	2.06 ± 0.02	$0.028^{+0.007}_{-0.008}$	$1.8^{+1.7}_{-1.3}$	1.13
BKNPL+SMC	$\Gamma_2 - 0.5$	$0.0024^{+0.0003}_{-0.0005}$	$2.07^{+0.05}_{-0.03}$	$0.030^{+0.007}_{-0.014}$	$1.8^{+1.7}_{-1.3}$	1.30

Notes.—Results of fits to the near-IR/optical/UV/X-ray SED at 4.26 days since trigger, with power-law and broken power-law continuum models absorbed by MW-, LMC-, and SMC-like extinction and by X-ray absorption assuming solar metallicity. Galactic absorption and extinction were fixed at $N_{H,Gal} = 4.8 \times 10^{20}$ cm^{-2} and $E(B-V) = 0.052$ mag, respectively, and only intrinsic (at $z = 1.547$) quantities are reported in the table. PL = power law (where $\Gamma = 1 + \beta$); BKNPL = broken power law; MW = Milky Way extinction curve; LMC = Large Magellanic Cloud extinction curve; SMC = Small Magellanic Cloud extinction curve (as parameterized by Pei 1992).

extracted such that the log midpoint coincided with that of the optical SED described above. The *Swift* XRT X-ray spectrum was extracted using the method stated in § 2.1.1 and with the same extraction regions. The UVOT fluxes were obtained using the conversions in Poole et al. (2008). We calculated the transmission through the Lyα forest for each optical and UV band (e.g., Madau 1995) adopting the spectral slope $\beta = 0.58$ derived from the optical SED, and we corrected for these factors: U transmission = 0.996, UVW1 = 0.848, UVM2 = 0.633, and UVW2 = 0.539. Galactic absorption and extinction were fixed at 4.8×10^{20} cm^{-2} (Dickey & Lockman 1990) and $E(B-V) = 0.052$ mag (Schlegel et al. 1998), respectively. The SED was created in count space following the method given by Starling et al. (2007) and having the advantage that no model for the X-ray data need be assumed a priori. We fit the SED using models consisting of an absorbed power law or absorbed broken power law with slopes free or tied to $\Gamma_1 = \Gamma_2 - 0.5$ as expected for a cooling break. X-ray absorption is modeled with the XSPEC model zphabs and assuming solar metallicity.

We find that a broken power law provides a significantly better fit to the continuum than a single power law. The difference in slope between the two segments of the power law when both are left to vary tends to that expected for a cooling break: $\Delta\Gamma = 0.5$. Fixing the difference in the power-law slopes to 0.5 confirms this. (When compared to the single power law, the improvement in fit is significant according to the F-test, with probabilities of 10^{-6} for MW, 10^{-9} for LMC, and 10^{-8} for SMC.) The cooling break can be well constrained to lie at 0.002 keV, 4.26 days since trigger. However, we caution that the distinction between the detection of a cooling break and a nondetection relies solely on the observed K-band flux, for which we have only two data points (see Table 1). Optical extinction is found to be $E(B-V) \approx 0.03$ mag (roughly equivalent to $A_V < 0.09$ mag), in full agreement with the fit from the optical SED alone. LMC and SMC extinction curves provide better fits than the MW extinction curve. The intrinsic X-ray absorption is relatively high, on the order of $N_H \approx 2 \times 10^{21}$ cm^{-2}. Details of the fits are presented in Table 4. The unfolded SED and best-fitting model (BKNPL+LMC) are shown in Figure 5.

3.4. *Light-Curve and SED Analysis*

The light curves at X-ray, UV, optical, and near-IR frequencies, as well as the SED spanning this large frequency range, can be utilized to determine the energy power-law index p of the electrons emitting the synchrotron radiation. Adopting the standard blast wave model, the temporal and spectral indices, α and β (respectively), can be expressed in terms of p (Zhang & Mészáros 2004), assuming either a homogeneous or stellar wind–like circumburst medium. A single power-law fit to the X-ray light curve after the flare at 1.5×10^5 s results in a temporal index of $\alpha_X = 1.68^{+0.19}_{-0.15}$. For the analysis of the optical temporal slopes we take the fits without the flares (see Table 2), i.e., $\alpha_{opt} = 1.56 \pm 0.27$ before the break and $\alpha_{opt} = 2.47 \pm 0.13$ after the break.

The SED fits suggest that there is a cooling break at 0.002 keV (i.e., in the R band) 4.26 days after trigger. However, this result should be interpreted with caution, since there is no achromatic light-curve break across the optical bands observed and the K-band flux is the only one that discriminates between presence or absence of a cooling break in the optical regime. Furthermore, the value of p one can derive from the spectral slope above the tentative cooling break is $2\beta + 1 = 2.12 \pm 0.02$, which is not in agreement with the values one obtains from the X-ray temporal slope, $p = (4\alpha_X + 2)/3 = 2.91^{+0.25}_{-0.20}$, and from the optical temporal slope in the case of a homogeneous circumburst medium, $p = (4\alpha_{opt} + 3)/3 = 3.08 \pm 0.36$. If the circumburst medium is structured like a stellar wind, $p = (4\alpha_{opt} + 1)/3 = 2.41 \pm 0.36$ from the optical temporal slope is in agreement with the spectral slope, but the X-ray temporal slope remains inconsistent. Such a discrepancy is not unprecedented (e.g., Perley et al. 2008). However, we can derive an interpretation that is consistent with both the spectral and temporal fits (see below).

If one adopts the single power-law fit to the SED, all of the observed bands are either in between or above the peak frequency ν_m and cooling frequency ν_c. One then finds that $p = 2\beta + 1 = 2.98 \pm 0.02$ or $p = 2\beta = 1.98 \pm 0.02$, respectively.

If one assumes that $\nu_m < \nu_X < \nu_c$, p is equal to $(4\alpha_X + 3)/3 = 3.24^{+0.25}_{-0.20}$ or $(4\alpha_X X + 1)/3 = 2.57^{+0.25}_{-0.20}$, for a homogeneous or windlike medium, respectively; if $\nu_m < \nu_c < \nu_X$, $p = (4\alpha_X X + 2)/3 = 2.91^{+0.25}_{-0.20}$. Comparing these values for p with the ones from the single power-law SED fit, it is clear that they are only consistent for $\nu_m < \nu_X < \nu_c$ and a homogeneous medium.

The prebreak optical temporal slope results in values for p of $(4\alpha_{opt} + 3)/3 = 3.08 \pm 0.36$ ($\nu_m < \nu_O < \nu_c$ and homogeneous medium), $(4\alpha_{opt} + 1)/3 = 2.41 \pm 0.36$ ($\nu_m < \nu_O < \nu_c$ and stellar wind medium), and $(4\alpha_{opt} + 2)/3 = 2.75 \pm 0.36$ ($\nu_m < \nu_c < \nu_O$). Comparing these values for p with the values from the SED fit, again $\nu_m < \nu_O < \nu_c$ and a homogeneous medium, which is the preferred situation from the X-ray temporal analysis, is consistent.

Concluding, the X-ray to infrared bands at ~4 days are situated in between ν_m and ν_c, with $p \approx 3$, and the circumburst medium is homogeneous. We note that the p-value we derive for GRB 070125 lies at the high end of the observed distribution and is similar to that measured for, e.g., GRB 980519 ($p = 2.96^{+0.06}_{-0.08}$; Starling et al. 2008). Starling et al. (2008) showed that the p-distribution for a subsample of *BeppoSAX* GRBs is inconsistent with a single value of p for all bursts at the 3 σ level, and they constrain the intrinsic width of the parent distribution of p-values to $0.03 < \sigma_{\rm scat} < 1.40$ (3 σ). A similar result was obtained for a *Swift* GRB subsample by Shen et al. (2006). If we adopt a mean observed p-value of 2.04, as measured for the *BeppoSAX* subsample, then $p = 3$ lies within the expected observational scatter.

3.5. *Rebrightening Episodes*

From the light curve (Fig. 2), we find evidence for two rebrightening or flaring episodes. These occur at $t = 1.15$ days (as observed by the Bok telescope, SARA, TNT, and KAIT) and $t = 1.36$ days (as observed by TNT and UVOT). The episode at $t = 1.15$ days is the best sampled, as illustrated by the Bok data in Figure 6. From the V band alone, we derive a change in magnitude of about 0.5 (corresponding to a 56% increase in flux) over a time period of $\Delta T \approx 8000$ s (0.093 days), or an average increase in flux density of 17.1 μJy hr^{-1}.

Rebrightening episodes are not an uncommon afterglow phenomenon and have been attributed to a variety of causes, including density fluctuations in the external medium (clumps, turbulence, or wind termination shock structures), energy injection episodes (refreshed shocks) from the catch-up of faster shells in the outflow, patchy shells leading to angular inhomogeneities, extended activity of the central engine, multicomponent jets, or, in rare cases, microlensing; see the recent summary by Nakar & Granot (2007) for links to the original literature on these options. Nakar & Granot (2007) reconsidered the density fluctuation model with detailed numerical simulations and find that sharp rebrightening episodes with $\Delta T/T < 1$ cannot be explained within this model. This result is in conflict with earlier conclusions, and the authors argue that their treatment of the reverse shock and photon travel-time effects explain the different outcome of their study.

The rebrightening episodes seen in GRB 070125 resemble those observed in GRB 021004 (de Ugarte Postigo et al. 2005; Pandey et al. 2003; Fox et al. 2003; Bersier et al. 2003; Uemura et al. 2003a), where three episodes with $\Delta T/T < 1$ are noted at $t \approx 0.05$, 0.8, and 2.6 days. The preferred interpretation for these episodes is fluctuations in the energy surface density, i.e., a patchy shell model (Granot & Königl 2003; Nakar & Oren 2004).

Another burst that lends itself to a comparison to GRB 070125 is the well-sampled "bumpy ride" event GRB 030329. Late-time energy injection ("refreshed shocks") has been invoked to explain the "bumps" in this GRB (Granot et al. 2003). The well-resolved rebrightening episode discussed here is thus not likely caused by density fluctuations in the circumburst medium, but more likely attributed to angular or temporal energy fluctuations. Recently, Jóhannesson et al. (2006) presented a detailed analysis of relativistic fireballs with discrete or continuous energy injection and showed that energy injection imprints significant features on the afterglow and thus provides a valuable diagnostic tool to study GRB fireball physics beyond the single-explosion standard model. In particular, Jóhannesson et al. (2006) find that refreshed shocks from a discrete injection episode at $t = 1.4$ days (with an energy twice that of the initial energy injection) may, if not delivered uniformly across the shock surface (i.e., if a patchy shell is assumed), explain the sharp bump at $t = 3.5$ days observed in GRB 000301C. A more detailed follow-up paper is planned to further explore the rebrightening episodes found in GRB 070125.

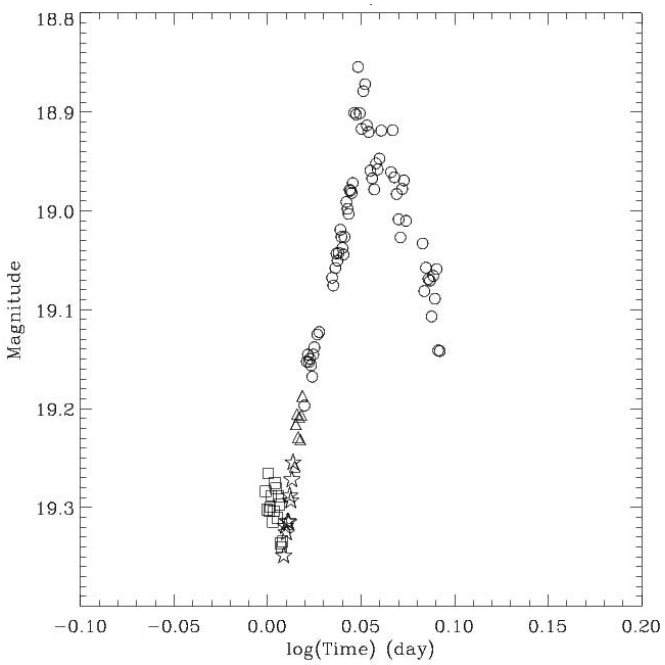

FIG. 6.—Bok *BVRI* data shifted to the V band, showing high-S/N detection of the second rebrightening episode, which has been confirmed by KAIT, TNT, and SARA data.

3.6. *Radio Light Curve*

The WSRT light curve at 4.8 GHz (see Fig. 3) displays the typical radio afterglow light-curve characteristics (e.g., Frail et al. 1997; Sari 1998). Except for the first measurement, all the observations were performed after the jet break time we derived from the optical light curves. At early times, the radio bands are situated below the synchrotron self-absorption frequency ν_a and the peak frequency ν_m. Since these two characteristic frequencies move to lower observing frequencies in time, the light curve first rises up to the jet break, after which the flux remains constant. The measurements at 1.5 and 5.6 days seem to deviate from this behavior, but this can be explained by the effect of radio scintillation (Goodman 1997). The rise in flux after ~40 days is caused by the passage of ν_m through the observing band, and the turnover at ~90 days by the passage of ν_a, after which the light curve declines quite steeply with a temporal index equal to the electron energy power-law index $p \approx 3$. More detailed modeling of the radio light curve will be presented in a follow-up paper.

3.7. *Spectroscopy*

It is evident from Figure 7 that the spectrum taken on 2007 January 26 at 05:44:05 is nearly featureless. We have convolved the spectrum with a Gaussian matched to the instrumental resolution and derive 4 σ equivalent width limits of approximately 10 Å at 3100 Å, 5 Å at 3200 Å, 3 Å at 3400 Å, 1.5 Å at 4000 Å, and 1 Å redward of 6000 Å. We identify only a few features at 4 σ statistical significance[34] as listed in Table 5.

Cenko et al. (2008) have reported the detection of a relatively weak Mg II doublet ($W_{\rm Mg\,II} < 1$ Å) in their afterglow spectrum of

[34] Note that systematic errors (e.g., continuum fitting) imply that the true significance limit is approximately 3 σ.

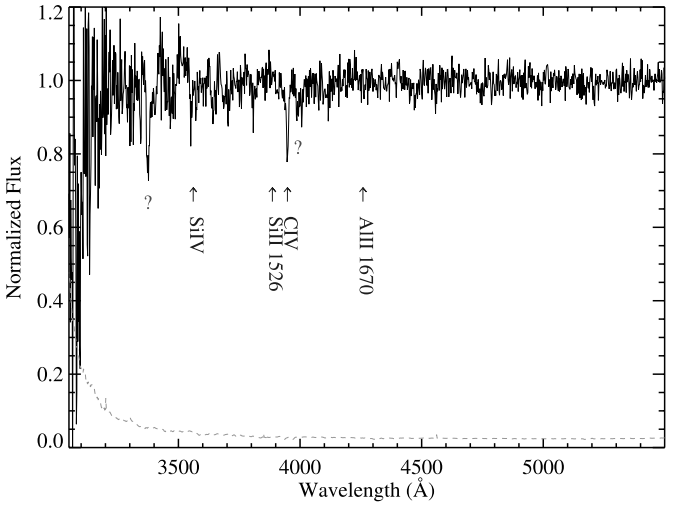

FIG. 7.—Normalized Keck LRIS spectrum of the afterglow of GRB 070125. The figure shows the data acquired with the blue camera using the 400/3400 grism. The labeled arrows identify transitions associated with the metal absorption system at $z = 1.547$. This gas most likely arises in the host galaxy of GRB 070125. We also mark several significant absorption features that remain unidentified. [*See the electronic edition of the Journal for a color version of this figure.*]

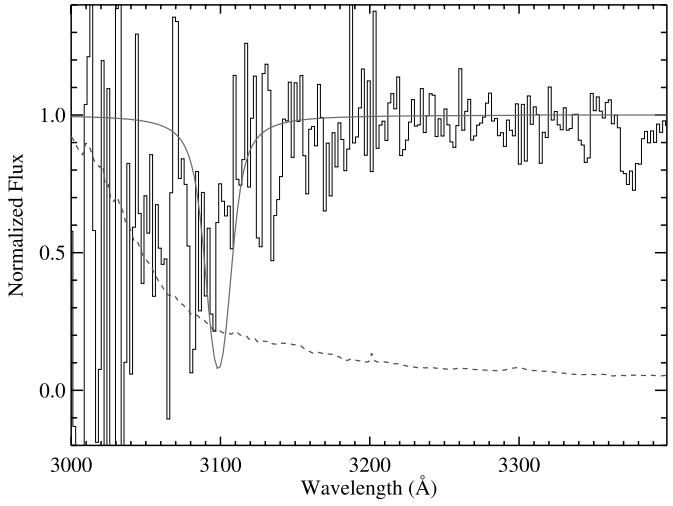

FIG. 8.—Close-up view of the spectral region near 3100 Å for the normalized Keck LRIS spectrum of the GRB 070125 afterglow. The dotted line indicates the 1 σ statistical error. The gray solid line traces a DLA profile with $N_{\rm H\,I} = 10^{20.3}$ cm^{-2} centered at the redshift of the observed metal-line absorption system ($z = 1.547$; Fig. 7). The data are formally inconsistent with a DLA feature at this redshift, but we caution that systematic uncertainties (wavelength calibration and continuum placement error) do not rule out such a profile at very high confidence (>99% c.l.). The data do rule out the presence of a strong Lyα absorber ($W_{\rm Ly\alpha} > 5$ Å) redward of 3140 Å. Furthermore, there is no obvious signature of the Lyα forest in this spectrum. For these reasons, we argue that the metal-line absorber at $z = 1.547$ is gas associated with the host galaxy of GRB 070125. We cannot rule out, however, the possibility that the feature at $\lambda \approx 3375$ Å is relatively weak Lyα absorption at $z = 1.78$. This sets a formal upper limit to the redshift of GRB 070125. [*See the electronic edition of the Journal for a color version of this figure.*]

GRB 070125, leading to an implied redshift of 1.547. Our spectra do not confirm this line measurement, but the reported equivalent width lies below our detection threshold. However, we identify a strong feature at 3947.1 Å, which corresponds to the expected position of the C IV doublet for $z = 1.547$. C^{+3} gas is frequently associated with Mg II absorbers (Churchill et al. 2000) and also gas surrounding GRB host galaxies (e.g., Mirabal et al. 2003). Unfortunately, we lack the spectral resolution to resolve the C IV doublet, but the likelihood of a misidentification is very low given the paucity of absorption lines in our data set. Furthermore, we observe weak absorption at the expected position of the Si IV doublet for $z = 1.547$, which is spectrally resolved (Fig. 7) but has less than 4 σ statistical significance. Altogether, the spectrum provides strong evidence for a metal-line absorption system at $z = 1.547$, especially given the independent report of Mg II absorption by Fox et al. (2007). In turn, we establish this redshift as the lowest possible value for GRB 070125.

Of principal interest to our study is whether this metal-line absorption system results from gas in the GRB host galaxy and therefore establishes the redshift of GRB 070125. There are two indisputable signatures that an absorption system corresponds to a GRB host galaxy: (1) One observes fine-structure levels of O^0, Si^+, or Fe^+. These transitions, which have never been detected in an intervening system with quasar absorption line spectroscopy, are known to arise from indirect radiative pumping by the GRB afterglow (Prochaska et al. 2006; Vreeswijk et al. 2007). (2) One positively identifies the Lyα forest imprint of the intergalactic medium and associates the highest redshift Lyα absorption with the GRB. In the latter case, one frequently observes a damped Lyα (DLA) profile[35] at the GRB redshift (Jakobsson et al. 2006).

Our spectrum reveals neither of these two signatures. First, we note no significant absorption from even the resonance lines of O^0, Si^+, or Fe^+, and we place relatively stringent upper limits on their equivalent widths (Table 5). Second, our spectrum does not unambiguously show the Lyα forest. Figure 8 presents the spectral region at $\lambda < 3400$ Å. Overplotted on the data (*solid gray line*) is a DLA profile centered at $z = 1.547$ assuming $N_{\rm H\,I} = 10^{20.3}$ cm^{-2}. Although the data formally reject the presence of a DLA system at this redshift, we caution that systematic effects (wavelength calibration, continuum placement) are not sufficiently large at $\lambda < 3100$ Å to rule out a DLA profile at >99% c.l. The data do, however, rule out a DLA profile at all wavelengths greater than 3140 Å.

The absence of a strong DLA system or an obvious series of Lyα absorption lines (i.e., the Lyα forest) places an upper limit on the redshift of GRB 070125. A reasonable estimate is to designate the absorption line (presently unidentified) at $\lambda = 3375$ Å as a Lyα transition and set $z_{\rm GRB} \leq 1.78$. The identification of this feature as Lyα is not supported by any coincident metal-line absorption (e.g., C IV). Furthermore, the implied rest equivalent width, $W_{\rm Ly\alpha} = 1.4$ Å, would be significantly lower than any thus far reported for gas surrounding a GRB. Nevertheless, we cannot rule out this interpretation altogether. Applying Occam's razor to our full set of observations, we associate the metal-line absorption

TABLE 5
ABSORPTION LINES

$\lambda_{\rm obs}$ (Å)	W_λ[a] (Å)	Transition	$\lambda_{\rm rest}$ (Å)	$z_{\rm abs}$
3316.6.....	<2.766	O I λ1302	1302.168	1.5470
3375.3.....	3.838 ± 0.706	...	...	...
3549.9.....	<1.810	Si IV λ1393	1393.755	...
3888.5.....	<1.180	Si II λ1526	1526.707	1.5470
3947.1.....	2.586 ± 0.318	C IV λ1548	1548.195	1.5495
		C IV λ1550	1550.770	1.5452
3989.2.....	1.501 ± 0.428	...	...	...
4096.7.....	<1.180	Fe II λ1608	1608.451	...
4255.5.....	<1.124	Al II λ1670	1670.787	1.5470

[a] Observed equivalent width.

[35] H I column density $N_{\rm H\,I} > 2 \times 10^{20}$ cm^{-2}.

system at $z = 1.547$ with the host galaxy of GRB 070125. To date, every absorption system that has been unambiguously associated with a GRB host galaxy (i.e., using the criteria above) has shown strong Lyα, Mg II, and C IV absorption. In fact, this afterglow spectrum would already represent the weakest Mg II doublet ever reported, although weaker C IV equivalent widths exist (Shin et al. 2006).

Whether or not we associate the $z = 1.547$ metal-line system with GRB 070125, this afterglow spectrum is remarkable in several respects. First, it is evident that the H I column density is low. Taking $z_{\rm GRB} = 1.547$, we have argued that the data prefer $N_{\rm H\,I} < 10^{20.3}$ cm^{-2}, which is a rare but not unprecedented result (Fynbo et al. 2005; Prochaska et al. 2005, 2006). If $z > 1.547$, then the Lyα transition has the lowest equivalent width reported for a GRB. Either way, the low $N_{\rm H\,I}$ value is remarkable given the expectation that the GRB progenitor arises in a high-density, star-forming region. Similar cases are discussed in Watson et al. (2007). Second, even taking $z_{\rm GRB} = 1.547$, the C IV, Mg II, and other low-ion equivalent widths are among the lowest observed to date for gas surrounding a GRB. Unfortunately, it is difficult to estimate the gas metallicity without a meaningful constraint on the $N_{\rm H\,I}$ value. Adopting $N_{\rm H\,I} = 10^{19}$ cm^{-2}, the upper limit to the equivalent width of Mg II λ2796 implies a Mg/H ratio less than 1/10 the solar value. We derive a similar value adopting the upper limit to the equivalent width of Si II λ1526 ($W_{1526}^{\rm rest} < 0.5$ Å) and assuming the metallicity/W_{1526} relation of Prochaska et al. (2008).

Taking both the spectroscopy and SED results into consideration, the host galaxy properties of GRB 070125 are consistent with those found in the sample presented by Fruchter et al. (2006).

4. IMPLICATIONS AND CONCLUSIONS

While we do not have data before 0.545 days (the first exposures were obtained in V with the UVOT), sampling thereafter is reasonably dense in time (see Fig. 2), until about 4 days after T_0. These observations suggest a possible jet break in the 1–3 day window. However, the strong variability (rebrightening episodes) around $t \approx 1$–2 days interferes with a clean detection of the jet break, and it is conceivable that the actual afterglow light curve is not best represented by a broken power law (the Beuermann-like profile) with superimposed "flares," but instead by three or more power laws, interrupted and perhaps reestablished by several periods of rebrightening. GRB 030329 provides an example of a GRB with a jet break at $t \approx 0.5$ days (Uemura et al. 2003b; Price et al. 2003), followed by multiple rebrightening episodes during subsequent days (e.g., Greiner et al. 2003; Lipkin et al. 2004). Given that the light curve of GRB 070125 exhibits strong variability, a jet break interpretation requires extreme care. However, the sparse late-time data do suggest that a break has occurred. Fitting the data past 2 days indicates that the actual jet break is more likely to be identified with the required change in slope at $t = 3.7$ days. If there indeed was no very early break in the optical power-law decay (before 0.5 days) and this late break time established from our fits is to be identified with the jet break, the indicated jet half-opening angle of 6.94° implies $E_\gamma = 6.93 \times 10^{51}$ ergs (from $E_{\rm iso,\,Konus}$), and GRB 070125 is consistent with the Ghirlanda relation (Ghirlanda et al. 2004).

The redshift allows us to place GRB 070125 in general context. Figure 9 shows the intrinsic afterglow of GRB 070125 in comparison with 52 other afterglows from the samples of Kann et al. (2006, 2007). These afterglows are in the R band and have been corrected for Galactic extinction and, where possible, for host galaxy and SN contributions. The afterglow of GRB 070125 was constructed by shifting BVI data to the R band, as only BV data are available at early times. Using the method described by

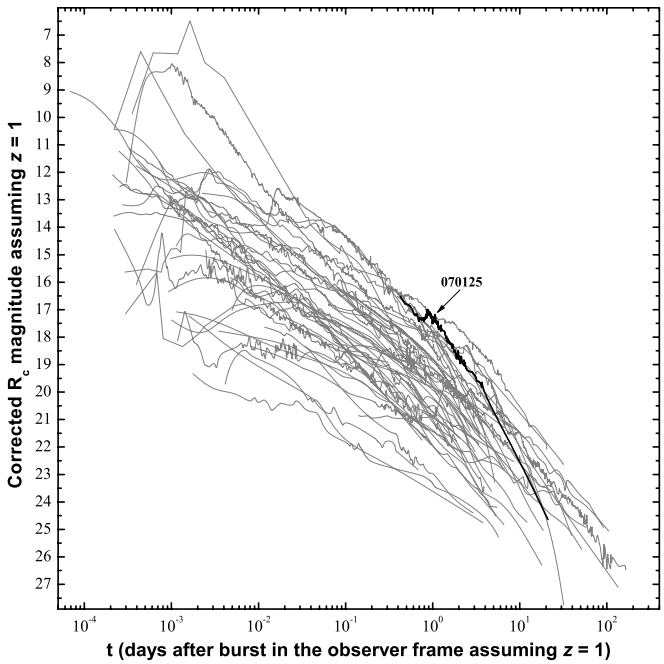

FIG. 9.—Afterglow light curves for 52 GRBs as they would look if all the bursts occurred at a redshift of 1 with no extinction (Kann et al. 2007). The thick line is the light curve of GRB 070125.

Kann et al. (2006), all afterglows have been corrected for rest-frame extinction and shifted to a common redshift of 1, allowing a direct comparison. The afterglow of GRB 070125 is found to be among the most luminous afterglows; at the time of the rebrightening at 1 day, only the afterglow of GRB 021004 is brighter. The afterglow properties thus corroborate the inferences we made in the previous section, where the beaming-corrected burst energy in the 1–10,000 keV regime (Bellm et al. 2007) was found to be on the high side of the observed statistical distribution.

Had GRB 070125 been much nearer, it would have given us an unprecedented opportunity to observe an afterglow on a much longer timescale, detect the additional emissions from an associated SN, and would have possibly revealed a host galaxy. At a redshift of 1.547, an unextinguished SN 1998bw would have peaked at $R \approx 27$ mag about 1 month after the burst. The LBT detection at late times could be explained with an SN like SN 1998bw, if one allows a scaling factor of $k = 2.25$, which is significantly larger than indicated by the properties of the sample of established GRB SNe (Zeh et al. 2005; Ferrero et al. 2006). In addition, assuming that the late-time detection is composed entirely of SN emission implies an even steeper afterglow decay. Given the uncertainties when extrapolating the light-curve properties of SN 1998bw to a redshift of 1.5, we caution that this factor has a large uncertainty. Based on what is known so far about the luminosities of GRB SNe (Zeh et al. 2004; Ferrero et al. 2006), it seems unlikely that the LBT data point is indeed representing SN light. Another alternative is light from an underlying host galaxy (not discernible in the images). Due to the second-epoch non-detection by the LBT (Dai et al. 2008), we can conclude that the host galaxy must be fainter than $M_V = 18.2$ mag ($R > 26.1$ mag), which is comparable to the Magellanic Clouds or even fainter (van den Bergh 2000), but consistent with the distribution found in the *Hubble Space Telescope* survey by Fruchter et al. (2006). The low metallicity we inferred from the spectra would also be consistent with a small, low-luminosity host galaxy.

GRB 070125 was unusual in several aspects. It had at least two sharp rebrightening episodes, it was intrinsically bright, and it did

not reveal the often associated DLA and Mg II features in its smooth spectrum. The collective efforts of a large group allowed us to learn much about this burst, but it also provides a good example of the all too common situation that the world resources are too scarce to follow every burst with the kind of intensity in time and bandpass that may be required to extract enough information about each burst. Bumps have to be resolved, light curves need to be followed over longer timescales with greater sampling frequency, SEDs need to be established at many epochs, the associated SNe should be checked even if the redshift is large, and host galaxy properties should be established. Global coverage is necessary so that bumps and jet breaks are not missed, especially if future missions, such as *EXIST* (Grindlay et al. 2006), may result in much higher burst rates.

A. C. U. and D. H. H. would like to thank Martha Leake and Matt Wood for generously sharing their SARA time with us. J. R. T. would like to acknowledge support from NSF grant AST 03-07413. D. A. K. and S. K. were supported by DFG grant Kl 766/13-2. J. P. H. acknowledges support from Swift Guest Investigator grant NNG06GJ25G. The work of P. W. A. R., D. N. B., and J. L. R. was sponsored at Pennsylvania State University by NASA contract NAS5-00136. Observations reported here were in part obtained at the MMT Observatory, a joint facility of the University of Arizona and the Smithsonian Institution. J. D., W. Z., and Y. Q. are supported by NSFC grant 10673014. E. M. and E. P. are members of the Collaborazione Italiana Burst Ottici (CIBO) and thank the staff astronomers of the TNG for the excellent support. Effort by C. W. H. was supported by a grant from NASA's Planetary Astronomy Program. R. L. C. S. acknowledges support from STFC. K. C. H. is grateful for IPN support under NASA grants NNG06GE69G and NNX06AI36G and under JPL contract 128043. The Westerbork Synthesis Radio Telescope is operated by ASTRON (Netherlands Foundation for Research in Astronomy) with support from the Netherlands Foundation for Scientific Research (NWO). A. J. v. d. H. was supported by an appointment to the NASA Postdoctoral Program at NSSTC, administered by Oak Ridge Associated Universities through a contract with NASA. A. V. F.'s group at UC Berkeley is supported by NSF grant AST 06-07485, NASA/*Swift* grant NNG06GI86G, the TABASGO Foundation, and the Sylvia and Jim Katzman Foundation. Some of the data presented herein were obtained at the W. M. Keck Observatory, which is operated as a scientific partnership among the California Institute of Technology, the University of California, and NASA. The Observatory was made possible by the generous financial support of the W. M. Keck Foundation.

REFERENCES

Barthelmy, S. D., et al. 2005, Space Sci. Rev., 120, 143
Bellm, E., Bandstra, M., Boggs, S., Wigger, C., Hajdas, W., Smith, D. M., & Hurley, K. 2007, GCN Circ., 6025, http://gcn.gsfc.nasa.gov/gcn/gcn3/6025.gcn3
Bellm, E. C., et al. 2008, ApJ, in press (arXiv:0710.4590)
Berger, E., Penprase, B. E., Cenko, S. B., Kulkarni, S. R., Fox, D. B., Steidel, C. C., & Reddy, N. A. 2006, ApJ, 642, 979
Bersier, D., et al. 2003, ApJ, 584, L43
Beuermann, K., et al. 1999, A&A, 352, L26
Bloom, J. S., Frail, D. A., & Kulkarni, S. R. 2003, ApJ, 594, 674
Bromm, V., & Loeb, A. 2006, ApJ, 642, 382
Burrows, D. N., et al. 2005, Space Sci. Rev., 120, 165
Cenko, S. B., & Fox, D. B. 2007, GCN Circ., 6028, http://gcn.gsfc.nasa.gov/gcn/gcn3/6028.gcn3
Cenko, S. B., Soderberg, A. M., Frail, D. A., & Fox, D. B. 2007, GCN Circ., 6186, http://gcn.gsfc.nasa.gov/gcn/gcn3/6186.gcn3
Cenko, S. B., et al. 2008, ApJ, 677, 441
Chandra, P., & Frail, D. A. 2007, GCN Circ., 6061, http://gcn.gsfc.nasa.gov/gcn/gcn3/6061.gcn3
Chandra, P., et al. 2008, ApJ, submitted (arXiv:0802.2748)
Churchill, C. W., Mellon, R. R., Charlton, J. C., Jannuzi, B. T., Kirhakos, S., Steidel, C. C., & Schneider, D. P. 2000, ApJ, 543, 577
Costa, E., et al. 1997, Nature, 387, 783
Curran, P. A., et al. 2007, MNRAS, 381, L65
Dai, X., et al. 2008, ApJ, 682, L77
Deng, J., & Zheng, W. 2006, Nuovo Cimento B, 121, 1469
de Ugarte Postigo, A., et al. 2005, A&A, 443, 841
Dickey, J. M., & Lockman, F. J. 1990, ARA&A, 28, 215
Fan, X., Carilli, C. L., & Keating, B. 2006, ARA&A, 44, 415
Ferrero, P., et al. 2006, A&A, 457, 857
Filippenko, A. V. 1997, ARA&A, 35, 309
Filippenko, A. V., Li, W. D., Treffers, R. R., & Modjaz, M. 2001, in ASP Conf. Ser. 246, Small Telescope Astronomy on Global Scales, ed. W. P. Chen, C. Lemme, & B. Paczyński (San Francisco: ASP), 121
Fox, D. B., Berger, E., Price, P. A., & Cenko, S. B. 2007, GCN Circ., 6071, http://gcn.gsfc.nasa.gov/gcn/gcn3/6071.gcn3
Fox, D. W., et al. 2003, Nature, 422, 284
Frail, D. A., Kulkarni, S. R., Nicastro, L., Feroci, M., & Taylor, G. B. 1997, Nature, 389, 261
Fruchter, A. S., et al. 2006, Nature, 441, 463
Fynbo, J. P. U., et al. 2005, ApJ, 633, 317
Galama, T. J., et al. 1998, Nature, 395, 670
Gallerani, S., Salvaterra, R., Ferrara, A., & Choudhury, T. R. 2008, MNRAS, 388, L84
Garnavich, P., et al. 2007, GCN Circ., 6165, http://gcn.gsfc.nasa.gov/gcn/gcn3/6165.gcn3
Gehrels, N., et al. 2004, ApJ, 611, 1005
Ghirlanda, G., Ghisellini, G., & Lazzati, D. 2004, ApJ, 616, 331
Goodman, J. 1997, NewA, 2, 449
Graham, J. A. 1982, PASP, 94, 244
Granot, J., & Königl, A. 2003, ApJ, 594, L83
Granot, J., Nakar, E., & Piran, T. 2003, Nature, 426, 138
Greco, G., et al. 2007, GCN Circ., 6047, http://gcn.gsfc.nasa.gov/gcn/gcn3/6047.gcn3
Greiner, J., et al. 2003, Nature, 426, 157
Grindlay, J. E., et al. 2006, in AIP Conf. Proc. 836, Gamma-Ray Bursts in the *Swift* Era, ed. S. S. Holt, N. Gehrels, & J. A. Nousek (New York: AIP), 631
Haislip, J., Reichart, D., Lacluyze, A., Ivarsen, K., Nysewander, M., Foster, A., & Crain, J. A. 2007, GCN Circ., 6044, http://gcn.gsfc.nasa.gov/gcn/gcn3/6044.gcn3
Haislip, J. B., et al. 2006, Nature, 440, 181
Hiltner, W. A. 1964, Astronomical Techniques (Chicago: Univ. Chicago Press)
Hjorth, J., et al. 2003, Nature, 423, 847
Hurley, K., et al. 2007, GCN Circ., 6024, http://gcn.gsfc.nasa.gov/gcn/gcn3/6024.gcn3
Jakobsson, P., et al. 2006, A&A, 447, 897
Jóhannesson, G., Björnsson, G., & Gudmundsson, E. H. 2006, ApJ, 647, 1238
Kann, D. A., Klose, S., & Zeh, A. 2006, ApJ, 641, 993
Kann, D. A., et al. 2007, ApJ, submitted (arXiv:0712.2186)
Kawai, N., et al. 2006, Nature, 440, 184
Klebesadel, R. W., Strong, I. B., & Olson, R. A. 1973, ApJ, 182, L85
Kouveliotou, C., Meegan, C. A., Fishman, G. J., Bhat, N. P., Briggs, M. S., Koshut, T. M., Paciesas, W. S., & Pendleton, G. N. 1993, ApJ, 413, L101
Kuin, N. P. M., & Rosen, S. R. 2008, MNRAS, 383, 383
Li, W., Filippenko, A. V., Chornock, R., & Jha, S. 2003, PASP, 115, 844
Li, W., Jha, S., Filippenko, A. V., Bloom, J. S., Pooley, D., Foley, R. J., & Perley, D. A. 2006, PASP, 118, 37
Lipkin, Y. M., et al. 2004, ApJ, 606, 381
Madau, P. 1995, ApJ, 441, 18
Malesani, D., et al. 2004, ApJ, 609, L5
McQuinn, M., Lidz, A., Zaldarriaga, M., Hernquist, L., & Dutta, S. 2007, MNRAS, submitted (arXiv:0710.1018)
Metzger, M. R., Djorgovski, S. G., Kulkarni, S. R., Steidel, C. C., Adelberger, K. L., Frail, D. A., Costa, E., & Frontera, F. 1997, Nature, 387, 878
Mirabal, N., Halpern, J. P., An, D., Thorstensen, J. R., & Terndrup, D. M. 2006, ApJ, 643, L99
Mirabal, N., et al. 2003, ApJ, 595, 935
Nakar, E., & Granot, J. 2007, MNRAS, 380, 1744
Nakar, E., & Oren, Y. 2004, ApJ, 602, L97
Oke, J. B., et al. 1995, PASP, 107, 375
Pandey, S. B., et al. 2003, Bull. Astron. Soc. India, 31, 19
Pei, Y. C. 1992, ApJ, 395, 130

Perley, D. A., et al. 2008, ApJ, 672, 449
Pian, E., et al. 2006, Nature, 442, 1011
Poole, T. S., et al. 2008, MNRAS, 383, 627
Price, P. A., et al. 2003, Nature, 423, 844
Prochaska, J. X., Chen, H.-W., Wolfe, A. M., Dessauges-Zavadsky, M., & Bloom, J. S. 2008, ApJ, 672, 59
Prochaska, J. X., Foley, R., Tran, H., Bloom, J. S., & Chen, H.-W. 2006, GCN Circ., 4593, http://gcn.gsfc.nasa.gov/gcn/gcn3/4593.gcn3
Prochaska, J. X., Foley, R. J., Chen, H.-W., Bloom, J. S., Hurley, K., Cooper, M., Guhathakurta, R., & Li, W. 2005, GCN Circ., 3971, http://gcn.gsfc.nasa.gov/gcn/gcn3/3971.gcn3
Racusin, J., Cummings, J., & Marshall, F. 2007a, GCN Rep., 28, 1
Racusin, J. L., Cummings, J., Marshall, F. E., Burrows, D. N., Krimm, H., & Sato, G. 2007b, GCN Rep., 28, 3
Rhoads, J. E., & Fruchter, A. S. 2001, ApJ, 546, 117
Roming, P. W. A., et al. 2005, Space Sci. Rev., 120, 95
Sari, R. 1998, ApJ, 494, L49
Sari, R., Piran, T., & Halpern, J. P. 1999, ApJ, 519, L17
Savaglio, S. 2006, New J. Phys., 8, 195
Schady, P., et al. 2007, MNRAS, 377, 273
Schlegel, D. J., Finkbeiner, D. P., & Davis, M. 1998, ApJ, 500, 525
Shen, R., Kumar, P., & Robinson, E. L. 2006, MNRAS, 371, 1441
Shin, M.-S., et al. 2006, ApJ, submitted (astro-ph/0608327)
Spergel, D. N., et al. 2007, ApJS, 170, 377
Stanek, K. Z., et al. 2003, ApJ, 591, L17
Starling, R. L. C., van der Horst, A. J., Rol, E., Wijers, R. A. M. J., Kouveliotou, C., Wiersema, K., Curran, P. A., & Weltevrede, P. 2008, ApJ, 672, 433
Starling, R. L. C., Wijers, R. A. M. J., Wiersema, K., Rol, E., Curran, P. A., Kouveliotou, C., van der Horst, A. J., & Heemskerk, M. H. M. 2007, ApJ, 661, 787
Tan, G. H. 1991, in IAU Colloq. 131, Radio Interferometry: Theory, Techniques, and Applications, ed. T. J. Cornwell & R. A. Perley (ASP Conf. Ser. 19; San Francisco: ASP), 42
Tegmark, M., et al. 2006, Phys. Rev. D, 74, 123507
Totani, T., Kawai, N., Kosugi, G., Aoki, K., Yamada, T., Iye, M., Ohta, K., & Hattori, T. 2006, PASJ, 58, 485
Uemura, M., Kato, T., Ishioka, R., & Yamaoka, H. 2003a, PASJ, 55, L31
Uemura, M., et al. 2003b, Nature, 423, 843
Updike, A. C., Hartmann, D. H., Bryngelson, G. L., Goldthwaite, R. C., & Puls, J. R. 2007, GCN Circ., 6029, http://gcn.gsfc.nasa.gov/gcn/gcn3/6029.gcn3
van den Bergh, S. 2000, Cambridge Astrophysics Series, 35
van der Horst, A. J. 2007a, GCN Circ., 6042, http://gcn.gsfc.nasa.gov/gcn/gcn3/6042.gcn3
———. 2007b, GCN Circ., 6063, http://gcn.gsfc.nasa.gov/gcn/gcn3/6063.gcn3
van Paradijs, J., et al. 1997, Nature, 386, 686
Vreeswijk, P. M., et al. 2007, A&A, 468, 83
Watson, D., Hjorth, J., Fynbo, J. P. U., Jakobsson, P., Foley, S., Sollerman, J., & Wijers, R. A. M. J. 2007, ApJ, 660, L101
Williams, G. G., Olszewski, E., Lesser, M. P., & Burge, J. H. 2004, Proc. SPIE, 5492, 787
Woosley, S. E., & Bloom, J. S. 2006, ARA&A, 44, 507
Yamaoka, K., et al. 2005, IEEE Trans. Nuc. Sci., 52, 2765
Zeh, A., Kann, D. A., Klose, S., & Hartmann, D. H. 2005, Nuovo Cimento C, 28, 617
Zeh, A., Klose, S., & Hartmann, D. H. 2004, ApJ, 609, 952
Zhang, B., & Mészáros, P. 2004, Int. J. Mod. Phys. A, 19, 2385